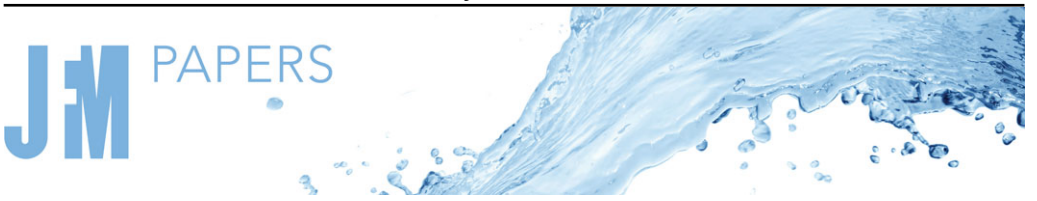
J. Fluid Mech. (2025), *vol.* 1007, A16, doi:10.1017/jfm.2025.28



Evolution of two-phase structures during the entire sandstorm process

Yanxiong Shi[1], **Hongyou Liu**[1] **and Xiaojing Zheng**[2]

[1]Center for Particle-laden Turbulence, Lanzhou University, Lanzhou 730000, PR China

[2]Research Center for Applied Mechanics, Xidian University, Xi'an 710071, PR China

Corresponding author: Hongyou Liu, liuhongyou@lzu.edu.cn

(Received 4 September 2024; revised 20 November 2024; accepted 22 December 2024)

The evolution of two-phase structures, turbulence/dust concentration structures, during an entire sandstorm process, including non-stationary flow, has been originally investigated in this study. Dust concentration structures are observed at different sandstorm stages, which are similar to the turbulence structures. These two-phase structures adhere to self-similarity in the steady stage but fail in the non-stationary stage. However, dust particle exhibits a better capability to follow eddies in flow, but the evolution of dust structures is not analogous to that of turbulence structures, exhibiting distinct trends. Dust particles, initiated from the ground, gradually form cluster structures in the rising stage. Their morphology exhibits a ridge-like evolutionary trend, reaching a peak in the steady stage. In contrast, turbulence structures are most persistent and oblique in the early stage but sequentially diminish in the subsequent steady and declining stages. The significant changes in shear due to sharply varying wind velocity and thermal stability are primarily responsible for these evolution differences.

Key words: atmospheric flows, particle/fluid flows, turbulent boundary layers

1. Introduction

Sandstorms are typically strong wind-blown-sand flows that have hysteretic, continuous and long-term effects on the environment, biology, climate and human activities and health (Mahowald *et al.* 2005; Lawrence & Neff 2009; Shao *et al.* 2013; Formenti *et al.* 2014; Lovett *et al.* 2018). Sandstorm formation and development are influenced by the interactions among atmospheric circulation, the local atmosphere, near-surface airflow and erodible surface materials (Knippertz 2014; Hamzeh *et al.* 2021; Miri *et al.* 2021; Gui *et al.* 2022). The analysis of a large amount of sandstorm data has suggested that there are rising and declining stages with obvious increasing or decreasing wind velocity where

© The Author(s), 2025. Published by Cambridge University Press.

https://doi.org/10.1017/jfm.2025.28 Published online by Cambridge University Press

the flow is non-stationary, as well as a steady stage where the wind velocity increases to reach a plateau that is maintained (Liu *et al.* 2022). Sandstorms are associated with intense mixing and transfer of mass and energy, in which coherent structures play a major role (Ginoux *et al.* 2001; Helmert *et al.* 2007; Choobari *et al.* 2012; Jacob & Anderson 2017). A coherent motion represents a region of a flow where at least one fundamental flow variable is highly correlated with itself or with another variable in both space and time (Robinson 1991). There are not only the turbulence structures but also dust concentration structures in the particle-laden flow/sandstorm, referred to as two-phase structures. The material–energy interactions in the non-stationary rising and declining stages are most intense and active in the sandstorm process (Barenblatt & Golitsyn 1974; Heinold *et al.* 2013; Kaskaoutis *et al.* 2019). However, existing studies on coherent structures have focused mainly on the characterization of the steady flow case, which is insufficient for a comprehensive description of the structure characterization in real geophysical flows (usually non-stationary). A detailed description of the evolution of morphological and dynamic characteristics of two-phase structures and their interaction throughout the entire sandstorm process, including the steady and non-stationary stages, is crucial for fully understanding of the spatial–temporal distribution and transport patterns of dust during sandstorms. This analysis also helps to establish a connection between microturbulence mechanisms and macroweather phenomena, thereby contributing to the development of an accurate model of sandstorm process.

Previous studies have demonstrated that turbulence coherent structures exist in wall-bounded turbulence, including channel (Zhou *et al.* 1999; Christensen & Adrian 2001; Monty *et al.* 2007), pipe (Kim & Adrian 1999; Bailey & Smits 2010; Baltzer *et al.* 2013) and atmospheric surface-layer (ASL) (Hutchins *et al.* 2012; Liu, Wang & Zheng 2017) flows. These structures include streaks, quasistreamwise vortices, hairpin vortices/hairpin vortex packets, large-scale motions (LSMs) and very large-scale motions (VLSMs or superstructures), where LSMs/VLSMs are usually regarded as the dominant structures in the outer region of the turbulence boundary layer (Marusic *et al.* 2010; Hutchins *et al.* 2012; Baltzer *et al.* 2013; Jiménez 2018; Liu & Zheng 2021). The spatial characteristic length scales and structure inclination angle have been widely investigated to quantify the morphological feature of these structures. Although the discovery of coherent structures in turbulence dates to as early as 1954 (Corrsin & Kistler 1955), it was not until 1970 that the existence of LSMs with streamwise length scales reaching up to 2–3δ (where δ denotes the boundary layer thickness) in the turbulent boundary layer was explicitly proposed by Kovasznay *et al.* (1970). Subsequently, VLSMs with streamwise length scales exceeding 3δ and even reaching 20δ at instantaneous times have been found in studies at higher-Reynolds-number flows (Kim & Adrian 1999; Adrian *et al.* 2000; Hutchins & Marusic 2007; Hutchins *et al.* 2012). Such VLSMs are present not only in particle-free flows, but also in particle-laden flows/sandstorms and contribute to the streamwise turbulent intensity reaches up to 60 % at the top of the logarithmic layer ($z/\delta = 0.2$) (Liu & Zheng 2021). These large-scale coherent structures in wall turbulence not only exhibit a large spatial extent, but also reportedly form an oblique angle with the wall along the streamwise direction, i.e. the structure inclination angle γ. Subsequent studies suggested that γ vary over a range of approximately $3°-35°$ (Kovasznay *et al.* 1970; Brown & Thomas 1977; Adrian *et al.* 2000; Christensen & Adrian 2001; Hommema & Adrian 2003; Marusic & Heuer 2007; Hutchins *et al.* 2012; Liu *et al.* 2020). Inclination angle have been demonstrated as a common feature of coherent structures in wall turbulence (Hommema & Adrian 2003; Marusic & Heuer 2007; Liu *et al.* 2020) and determines the pathways for the transport of quantities, such as heat, mass and momentum (Marusic *et al.* 2010;

https://doi.org/10.1017/jfm.2025.28 Published online by Cambridge University Press

Jacob & Anderson 2017). In addition, there is a self-similarity of coherent structures in the flow field that is described by the attached eddy model (Townsend 1976; Perry *et al.* 1986; Marusic & Monty 2019). The self-similarity indicates that the size of the hierarchical eddies scale as their distances from the wall in the logarithmic region (Baars *et al.* 2017), which was quantified in terms of a streamwise/wall-normal aspect ratio of $\lambda_x/z \approx 14$ in the particle-free flow (Baars *et al.* 2017; Krug *et al.* 2019; Duan *et al.* 2020; He *et al.* 2024).

The above studies on large-scale coherent structures mainly focused on near-neutral particle-free flows. However, the morphological characteristics of coherent structures in complex ASL flows are affected by various environmental factors. In the unstable ASL, the buoyancy effect could lead to larger inclination (Hommema & Adrian 2003; Carper & Porté-Agel 2004; Chauhan *et al.* 2013; Salesky & Anderson 2018; Liu *et al.* 2020; Li *et al.* 2022) and spatial length scale (Chauhan *et al.* 2010; Liu & Zheng 2024), but smaller aspect ratio (Krug *et al.* 2019). In the stable regime, the sinking cold and denser air exhibits a 'suppressing' effect that results in contrary phenomena with those in unstable regime in structure inclination angle (Chauhan *et al.* 2013; Liu, Bo & Liang 2017) and spatial length scale (Chauhan *et al.* 2010,2013; Liu & Zheng 2024), and the absence of self-similar scaling (Krug *et al.* 2019). The addition of sand/dust particles causes an increase in the structure inclination angle (Wang *et al.* 2020; He & Liu 2023) but a decrease in the streamwise length scale (Wang *et al.* 2020) and aspect ratio (He *et al.* 2024). In addition, the flow acceleration significantly enhances the near-wall Reynolds shear stresses, making the large-scale coherent structures more elongated (Talamelli *et al.* 2002).

Another characteristic of sandstorms is that, under the effect of sand/dust transport from upstream and local sand/dust emission by strong winds, the atmosphere is filled with large amounts of sand/dust particles, and the concentration remarkably increases. In particular, the increase in concentration of particles with sizes less than 10 μm (PM10) is the most significant (Behrooz *et al.* 2022). The spatial and temporal distributions of dust particles in wind-blown sand flows can be considerably affected by turbulence motions (Balachandar & Eaton 2010). Dust could be captured by turbulence structures and aggregate in the low vorticity high-shear region (Eaton & Fessler 1994; Yang *et al.* 2017; Lee & Lee 2019; Liu *et al.* 2020). In wall turbulence, quasistreamwise vortex structures and LSMs in the boundary layer affected the preferential aggregation of particles in the near-wall region (Marchioli & Soldati 2002) and dominated the formation of elongated large-scale particle cluster structures (Bernardini *et al.* 2013). The elongated particles streaky structure in the near-wall flow field (McLaughlin 1989; Kaftori *et al.* 1998) was verified as a visual footprint of LSMs/VLSMs (Wang *et al.* 2019). Monchaux *et al.* (2010) observed self-similarity of the geometries of particle clusters in a particle-laden grid turbulence, which was also noted by Zhu *et al.* (2021) in the particle-laden turbulent boundary layer and they found that particles cluster with each other under the high-strain effect contributed by these turbulence structures and evolve with them in a similar way. This indicates that the particle structures in the particle-laden turbulent boundary layer could have geometrical morphological features akin to those of turbulent structures (Monchaux *et al.* 2010; Zhu *et al.* 2021). Recently, very large-scale dust structures in the PM10 concentration field, which are similar to VLSMs in the flow field, were found by He & Liu (2023) based on the fluctuating PM10 concentration measured in wind-blown-sand flow and they noted that the dust clusters exhibited self-similarity akin to flow field structures (He *et al.* 2024).

In summary, the morphological characteristics of turbulence velocity/dust concentration structures including streamwise length scale, inclination angle and self-similarity, have attracted the attention of many researchers. However, existing studies mainly focused on the steady flow case, much less is known about the evolution of the coherent structure when

https://doi.org/10.1017/jfm.2025.28 Published online by Cambridge University Press

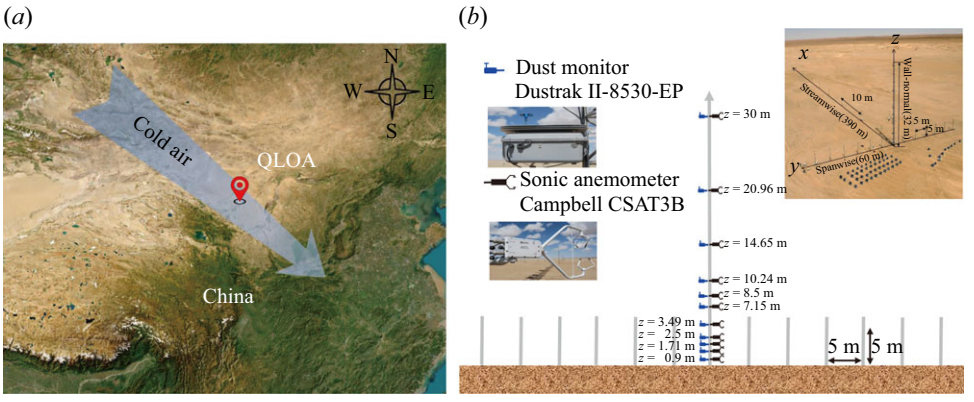


Figure 1. Location of the QLOA site and the layout of all instruments. (*a*) Satellite photographs of the QLOA site; (*b*) the sonic anemometers and dust monitors array on the wall-normal array, the inset is panoramic view of the QLOA.

the flow variables (such as the wind velocity and dust concentration) are continuously varied. We address this aspect here by investigating the continuously varying multipoint wind velocity and PM10 concentration data obtained from field observations during the entire sandstorm process. The hope is that these results will allow for a better understanding of how two-phase structures relate and affect one another. The remainder of this work is organized as follows. The experimental set-up for the field observations is described in § 2. In § 3, the existence of the large-scale two-phase structures during the sandstorm is verified. The evolution of morphological characteristics, including streamwise length scale, structure inclination angle and self-similarity of two-phase structures are presented in § 4. Finally, concluding remarks are outlined in § 5.

2. Experimental set-up and data preprocessing

The Qingtu Lake Observation Array (QLOA) is located on a flat dry lakebed at the edge of the vast desert in the Northwest China. The area encompasses a sandy surface, and lies on the path of cold air travelling through Northwest China (as shown in figure 1*a*). During the spring and winter seasons, East Asian cold air outbreaks can cause strong winds exhibiting relatively stable propulsion velocity and direction, resulting in frequent sandstorms in the area. Therefore, the QLOA is an ideal natural site for the study of wind-blown-sand flows/sandstorms with high Reynolds number. The site comprises 24 observation towers, where the main tower is 32 m high and the remaining towers are 5 m in height. These towers are arranged in a Cartesian coordinate system. Specifically, there are 11 towers along the northwest direction (prevailing wind direction, x-axis) and six spanwise towers on the left- and right-hand sides of the main tower (y-axis) (as shown in figure 1*b*). To capture wind velocity and PM10 concentration data during sandstorms, 11 sonic anemometers (Campbell CSAT3B) and the same number of aerosol monitors (TSI, Dustrak II-8530-EP) are installed on the main tower from 0.9 to 30 m in a logarithmic gradient. More details on the QLOA also can be found in (Wang & Zheng 2016; Liu & Zheng 2021).

In mid-April 2016, the average circulation over Eurasia turned into two troughs and one ridge. Under the combined influence of the westerly trough, plateau trough and south branch trough, there was a cold air process with a low trough moving eastward

https://doi.org/10.1017/jfm.2025.28 Published online by Cambridge University Press

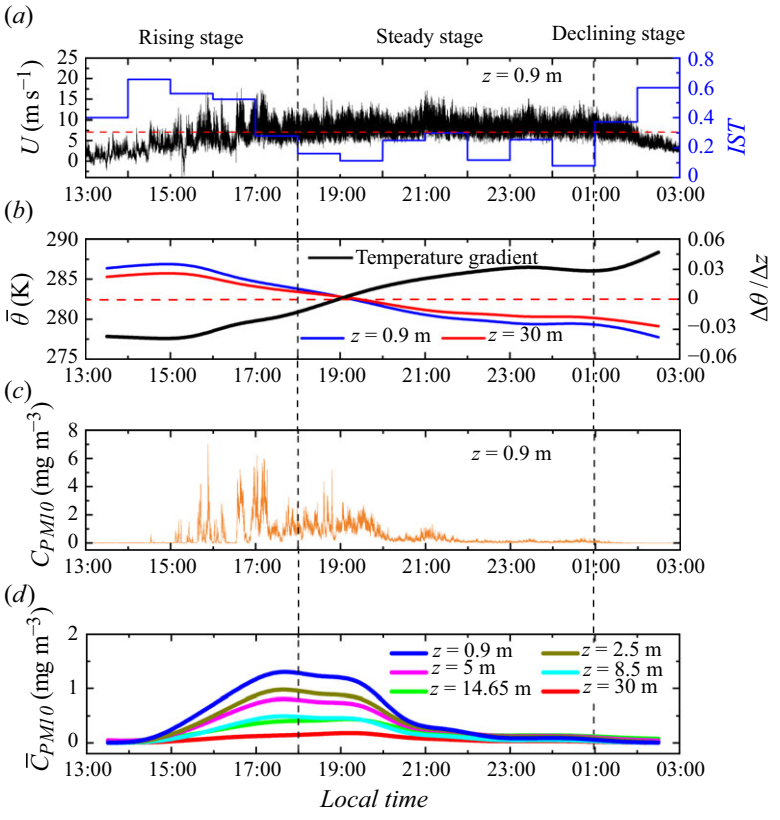


Figure 2. Data series during the sandstorm. (*a*) Streamwise velocity at a height of $z = 0.9$ m, where the blue line denotes the non-stationary index *IST*; (*b*) average ambient temperature and the temperature gradient from $z = 0.9{-}30$ m (black line); (*c*) PM10 concentration at a height of $z = 0.9$ m and (*d*) average PM10 dust concentration.

in Northwest China from 16–17 April (Liu *et al.* 2022). The upper-level jet stream caused intensely cold air to develop downward and transported a large amount of momentum, promoting the formation of a cold ground front in the QLOA area. The strong wind behind the front lifted sand/dust particles from the ground and culminated in a sandstorm event. The QLOA site captured the sandstorm event and recorded three-dimensional wind velocity, temperature and PM10 concentration data for the entire process. As shown in figure 2(*a*), the wind velocity in the observation area started to increase at 13:00 on 16 April. After five hours of development, the average wind velocity reached 8.5 m s^{-1} at a height of 0.9 m, and the steady strong winds lasted for approximately seven hours. The wind velocity then began to decrease at 01:00 on the next day, and the sandstorm event was basically over at 03:00 on 17 April. The changes in the local temperature shown in figure 2(*b*) reveal the thermal conditions of this sandstorm process. In the early stage of the sandstorm, the front of the cold air reached the observation area and encountered the local warm air. But due to solar radiation, the temperature slightly increased from 13:00 to 15:00 on 16 April. The ground temperature exceeded the upper air temperature; that is, there is an unstable stratification. At approximately 15:00, the cold air fully entered the observation area and mixed with local warm air. As a result, the local temperature dropped and the wind velocity continuously increased. Sand/dust particles on the ground

https://doi.org/10.1017/jfm.2025.28 Published online by Cambridge University Press

were entrained into the air by strong winds and the dust concentration in the ASL rapidly increased. The instantaneous PM10 concentration can reach up to 7.02 mg m^{-3} at a height of 0.9 m, as shown in figure 2(*c*). With sandstorm development, the difference in the air temperatures between the upper and near ground layer gradually decreased, and the atmospheric instability gradually weakened. Beginning at approximately 20:00 on 16 April, the upper-layer temperature began to be higher than that near ground, indicating that a thermal inversion layer appeared; namely, the atmosphere gradually turned into a stable condition. The suppressing effect of sinking cold and denser air result in weakened atmospheric diffusion and decreased in the PM10 concentration from 20:00. With the exit of the cold front event, the wind velocity gradually decreased from 01:00 on 17 April, and the PM10 concentration gradually decreased to zero, implying the end of this sandstorm event. Following Liu *et al.* (2022), the sandstorm process is divided into rising, steady and declining stages, corresponding to the processes of increasing, maintaining and decreasing wind velocities, with the durations of 5, 7 and 2 h, respectively.

As shown in figure 2(*a*), the non-stationary index IST ($IST = |(CV_m - CV)/CV|$, where $CV_m = \sum_{i=1}^{n} CV_i/n$, CV_i is the local variance in each segment of the data and CV is the overall variance in the signal) of the wind velocity series during the rising and declining stages of the sandstorm are less than 0.3, indicating that the wind velocity signal exhibits non-stationary characteristics (Foken *et al.* 2004). Therefore, the adaptive segmented stationary method proposed by Liu *et al.* (2022) was utilized in this study to analyse the non-stationary data. The method processes the non-stationary signals from the deterministic trend component and the stationary zero mean fluctuating component based on the Cramer decomposition theorem. On the one hand, the empirical modal decomposition is employed to extract the time-varying mean flow, where the fluctuations with period greater than one hour are considered as the time-varying mean wind velocity that represents the average trend of the wind field (Wyngaard 1992). On the other hand, an adaptive segmentation procedure is conducted for non-stationary fluctuating signals. First, the step interval duration is determined according to the characteristic time of typical energetic eddies in the outer region of the wall-bounded turbulence, i.e. $\triangle t = 10\delta/U_c$ (where U_c is the convection velocity taken as the local mean); second, stationarity and statistical convergence test are performed to determine adaptive segmented length of interval $\triangle T_i = k\triangle t$, where $k \in N^*$; finally, a non-stationary signal can be divided into several stationary segments

$$u(t) = \{u_1(\triangle T_1), u_2(\triangle T_2), \ldots, u_i(\triangle T_i), \ldots, u_m(\triangle T_m)\}, \tag{2.1}$$

where $t = \sum_{i=1}^{m} \triangle T_i$. Every segments $u_i(\triangle T_i)$ is stationary and can be used for statistical analysis. More details on the adaptive segmented stationary method can be found in Liu *et al.* (2022,2024). After using the method, the rising stage is divided into five segments with corresponding durations of 60, 55, 60, 80 and 45 min, the declining stage is divided into two segments with duration of one hour, and the steady stage is divided into seven hourly time series following standard practice in the analysis of ASL data (Wyngaard 1992). The change in mean wind velocity within each segment is small and the fluctuating is stationary. Moreover, the level of turbulence intensity (i.e. fluctuations compared with the mean wind value) is less than 0.1 at most of the position in the entire sandstorm process, which justify the approximation of the Taylor's hypothesis (Lin 1953). Subsequent analyses (two-point correlation, premultiplied spectra, streamwise length scale, structure inclination angle and linear coherence spectrum (LCS)) are performed for each stationary segments, and then the evolution of these features over the entire process of the dust storm is obtained.

https://doi.org/10.1017/jfm.2025.28 Published online by Cambridge University Press

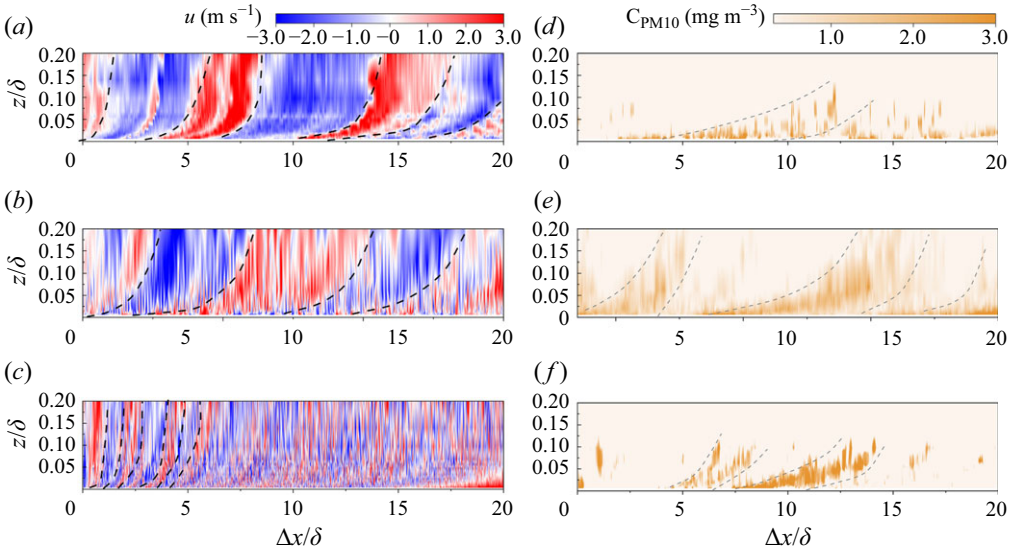


Figure 3. Instantaneous streamwise velocity fluctuations (*a–c*) and PM10 concentration fluctuations (*d–f*) in the streamwise/wall-normal planes in the different stages of sandstorms, where (*a*) and (*d*) show the rising stage results, (*b*) and (*e*) show the steady stage results and (*c*) and (*f*) show the declining stage results. The dashed lines denote the approximate boundaries of the high/low-speed regions and high/low-concentration regions.

3. Existence of the large-scale two-phase structures during the sandstorm

Turbulence coherent structures could cause continuous streamwise velocity deficit, creating a region where the streamwise velocity is lower than the mean convective velocity (Hutchins & Marusic 2007). The extent of low-speed fluid region is correlated with the instantaneous spatial extent of the turbulence coherent structures. Therefore, to investigate the existence of turbulence structures during the sandstorm, figure 3(*a–c*) show the instantaneous streamwise velocity fluctuations in the streamwise/wall-normal planes in the different stages of the sandstorm, where instantaneous time variation in u is projected in space by using Taylor's hypothesis and the convection velocity is taken as the local mean (Del Á Lamo & Jiménez 2009; Baidya *et al.* 2017; He & Liu 2023). There are alternating low-speed fluid regions (marked by blue) and high-speed fluid regions (marked by red) during the sandstorm, where the approximate boundaries of high/low-speed regions are manually marked with dashed lines. The streamwise extents of low-speed regions exceed 3δ in the steady stage, which is consistent with the existing results for particle-free/particle-laden flows (Hutchins *et al.* 2012; He & Liu 2023). However, there are significant differences in streamwise extents between the steady and declining stages, but not between the rising and steady stages. In the declining stage, the streamwise extent is smaller than that in the steady case and shorter than 3δ. This suggests that VLSMs may originally exist in the rising stage of sandstorms rather than gradually form, continue to be maintained in the steady stage, and disappear in the declining stage as the sandstorm attenuates.

Dust particles in the flow field will appear unevenly distributed in the influence of turbulent coherent structures (Balachandar & Eaton 2010). To clarify the preferential sampling of the sand concentration on specific flow structure, the joint probability density function (j.p.d.f.) of the streamwise velocity fluctuation u and PM10 concentration fluctuations c was perform,c σ. Figure 4 shows the j.p.d.f. at a height of 5 m, where

https://doi.org/10.1017/jfm.2025.28 Published online by Cambridge University Press

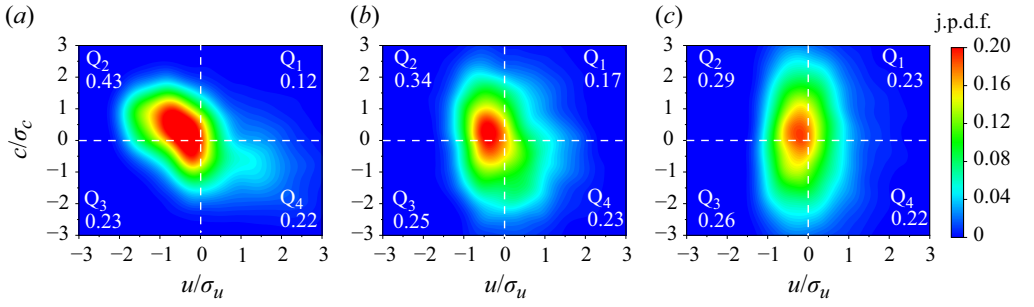


Figure 4. The j.p.d.f. of the streamwise velocity fluctuation u and PM10 concentration fluctuations c at a height of 5 m, where (a–c) correspond to the rising, steady and declining stages, respectively.

figure 4(a–c) correspond to the rising, steady and declining stages, respectively. The j.p.d.f tends to be a significant distribution with the long axis pointing to the second and fourth quadrants in the rising and steady. In the descending phase, the long axis changes parallel to the y-axis. To further quantify the distribution, the probability of each quadrant event is also calculated and marked in the corresponding quadrant in the figure. From its general trend, the probability of the Q2 event is larger than other events in each stage, i.e. positive c is highly correlated with negative u. This suggests that the dust particles aggregate in the low-speed region (low-momentum) and forming a high concentration region. Similar to the method of detecting turbulence structures through instantaneous flow fields, dust concentration structures can also be visualized through the instantaneous PM10 concentration fields. Notably, the same conversion method could be applied to the temporal variation in the PM10 concentration fluctuations. This could be considered reasonable because PM10 exhibits a better capability to follow eddies in flow (He & Liu 2023) and the particle-to-fluid relative velocity for the dust particles is nearly zero (Zhang & Zhou 2023). The instantaneous PM10 dust concentration field in figure 3(d–f) show that there are high/low-concentration regions that are similar to the high/low-speed regions. As shown in figure 3(e), the extent of the high-concentration region (marked in yellow) in the steady stage exceeds 3δ along the streamwise direction and is comparable in order of magnitude to that of the low-speed regions in the steady stage. This indicates that large-scale structures with exceeding 3δ exist not only in the flow field but also in the dust concentration field and the scale of large-scale dust cluster structures is comparable in order of magnitude to that of the largest turbulence structures, which is consistent with the results from Bernardini *et al.* (2013) and He & Liu (2023). Although high-concentration regions can be found in the rising stage, the streamwise extent is significantly smaller than that in the steady stage, which is different from the case in instantaneous flow field. This implies that there may be a significant difference in the formation process and mechanism between dust and turbulence structures in the rising stage and this difference also causes the streamwise extent of the high-concentration regions to be significantly smaller than that of the low-speed regions in the rising stage. In the declining stage, the high-concentration regions gradually disappear as the sandstorm attenuates, as do the low-speed regions. In addition, the high-concentration regions only emerged near the ground in the rising and declining stages, which may be associated with the spatial transport contribution of wall-normal velocity.

The instantaneous streamwise velocity/concentration fluctuations represent a moment of turbulence/dust concentration coherent structures, but the two-point correlation can determine the average structure characteristics and reflect the statistical significance

https://doi.org/10.1017/jfm.2025.28 Published online by Cambridge University Press

of these structures. For fluctuating signals $P(t_0)$ and $Q(t)$ acquired at two space points $A(x_0, y_0, z_0)$ and $B(x_0, y_0, z_0)$ (the fluctuating signal can be streamwise velocity fluctuations u, and PM10 concentration fluctuations c). The relative temporal lead/lag is referred to as $\triangle t = t - t_0$. Then, the space–time cross-correlation of P and Q is defined as

$$R_{PQ}\,(x_0, x, y_0, y, z_0, z, t_0, t) = \frac{\langle P\,(x_0, y_0, z_0, t_0)\,Q(x, y, z, t)\rangle}{\sigma_{P(x_0,y_0,z_0,t_0)}\sigma_{Q(x,y,z,t)}} \tag{3.1}$$

where the angule brackets indicate a long time average and σ denotes the root-mean-square of the fluctuating signal. For signals measured at different height points, the spatial characteristics along the flow direction can be obtained from the time correlation of the time series through Taylor's hypothesis, and those along the height can be obtained from the two-point correlation of the fluctuating signals acquired at different locations at the height, i.e.

$$\begin{aligned} R_{uu}(\triangle x, y, \triangle z) &= \frac{\langle u\,(x_0, y_0, z_0)\,u\,(x_0 + U_c\triangle t, y, z_0 + \triangle z)\rangle}{\sigma_{u(x_0,y_0,z_0)}\sigma_{u(x_0+U_ct,y,z_0+\triangle z)}} \\ &= \frac{\langle u\,(x_0, y_0, z_0)\,u\,(x_0 + \triangle x, y, z_0 + \triangle z)\rangle}{\sigma_{u(x_0,y_0,z_0)}\sigma_{u(x_0+\triangle x,y,z_0+\triangle z)}} \end{aligned} \tag{3.2}$$

and

$$\begin{aligned} R_{cc}(\triangle x, y, \triangle z) &= \frac{\langle c\,(x_0, y_0, z_0)\,u\,(x_0 + U_c\triangle t, y, z_0 + \triangle z)\rangle}{\sigma_{c(x_0,y_0,z_0)}\sigma_{u(x_0+U_ct,y,z_0+\triangle z)}} \\ &= \frac{\langle c\,(x_0, y_0, z_0)\,c\,(x_0 + \triangle x, y, z_0 + \triangle z)\rangle}{\sigma_{c(x_0,y_0,z_0)}\sigma_{c(x_0+\triangle x,y,z_0+\triangle z)}} \end{aligned} \tag{3.3}$$

where U_c is the convection velocity taken as the time mean of the velocities at different heights. Isocontours of the streamwise velocity and dust concentration fluctuations are shown in figure 5, where the reference height is $z_{ref} = 0.006\delta$; that is, two-point correlation analysis is conducted using the signals obtained from the lowest measurement point and higher wall-normal positions. There are regions of positive correlation R_{uu} with large spatial extent that are associated with the morphological characteristic of coherent structures in both the flow and dust concentration fields during the sandstorm, but a significant extent difference can be observed at different stages. Figure 5(*a–c*) show that the streamwise extent of the positive correlation regions in the flow field is largest in the rising stage, second largest in the steady stage and smallest in the declining stage. Specifically, the streamwise extent of the positive correlation regions is larger than 3δ in the steady stage, indicating that there are VLSMs as reported in previous documents (Hutchins *et al.* 2012; He & Liu 2023). The streamwise extent in the rising stage not only exceeds 3δ, but also is more persistent in the streamwise direction than that in the steady stage. This indicates that the coherent structures in the rising stage is larger than those in the steady stage. Compared with those in other two stages, the positive correlation region is significantly reduced and smaller than 3δ in the declining stage, i.e. VLSMs disappear in the declining stage. As shown in figure 5(*d–f*), the positive correlation regions in the dust concentration field are increasing and then decreasing, indicating that the dust concentration structures emerge gradually with sandstorm development, reach a plateau in the steady stage and dissipate in the declining stage. The positive correlation region with streamwise extent exceeding 3δ in the steady stage provides further evidence of the existence of a very large-scale dust concentration structures similar to VLSMs. However, comparing figure 5(*b,e*), the dust structures are larger than the turbulence structures at

https://doi.org/10.1017/jfm.2025.28 Published online by Cambridge University Press

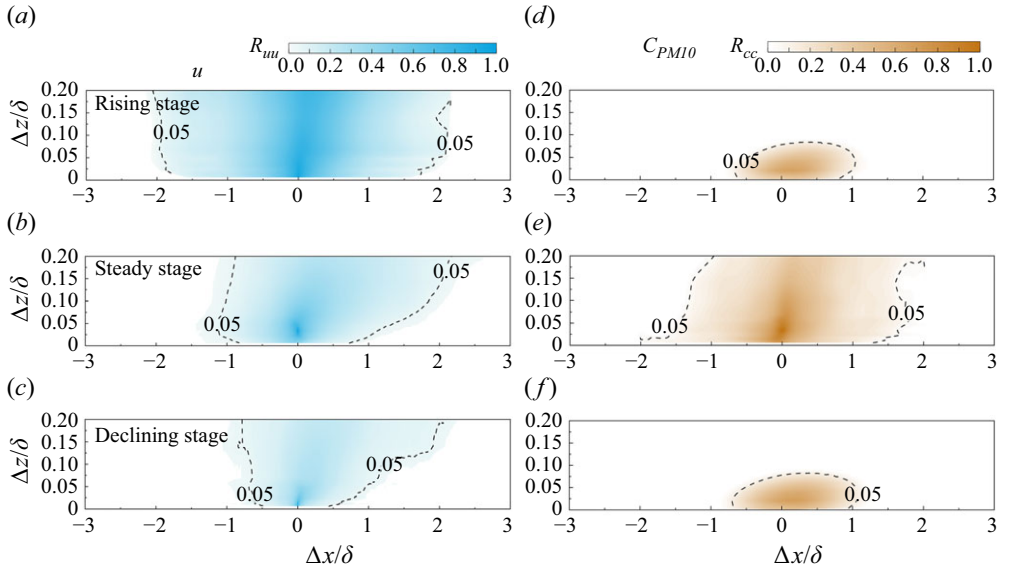


Figure 5. Two-dimensional correlation contours of the streamwise velocity fluctuations (*a–c*) and PM10 concentration fluctuations (*d–f*) in the streamwise/wall-normal planes in the different stages of sandstorms, the layout is the same as that in figure 3. The dashed lines denote a correlation coefficient of 0.05.

lower positions, and the difference decreases with height. This is similar to the two-point correlation of fluid and scalar in the transport of the tracer gas plume Talluru *et al.* (2018) and in the particle-laden flow (He & Liu 2023). In the rising and declining stages, the positive correlation regions are smaller than in the steady stage and occur only in near-ground regions, which differs from that in flow field. This further proves that the formation and disappearance mechanisms of dust structures are different from those of turbulent structures. The calculated correlation contours depicted in figure 5 provide statistical support for the instantaneous pattern of the coherent structures shown in figure 3. In addition, the correlation contours in figure 5 show a clear inclination along the streamwise direction, suggesting that these structures have an oblique angle to the free stream (Kovasznay *et al.* 1970; Ganapathisubramani *et al.* 2005; Marusic & Heuer 2007; Liu *et al.* 2017*a*; He & Liu 2023).

The instantaneous streamwise velocity/concentration fluctuations and the two-point correlation contours reflect the spatial morphological features of coherent structures. The premultiplied spectra could further show the distribution of energy between the multiscale turbulence structures and reflect the importance of coherent structures in terms of energy contribution. Therefore, figure 6 shows contour maps of the premultiplied spectra of the streamwise velocity fluctuations ($k_x\Phi_{uu}/u_\tau^2$) and dust concentration fluctuations ($k_x\Phi_{cc}/\sigma_c^2$), where $k_x = 2\pi/\lambda_x$ is the streamwise wavenumber; λ_x is the streamwise wavelength; Φ_{uu} and Φ_{cc} are the power spectral densities of the streamwise velocity and dust concentration fluctuations, respectively; u_τ is the friction velocity. The calculation of the premultiplied spectrum follows the methods of Kim & Adrian (1999) and Kunkel & Marusic (2006). The lower wavenumber peaks that are associated with the most significant energetic structures are also shown by white filled symbols. It can be seen that the premultiplied spectra are ridge-like across the observation ranges. However, the difference is that the wavelengths corresponding to the energy peaks and their variation with height vary considerably at different stages. As shown in figure 6(*b*), in the steady stage, $(\lambda_{ux})_{max}$

https://doi.org/10.1017/jfm.2025.28 Published online by Cambridge University Press

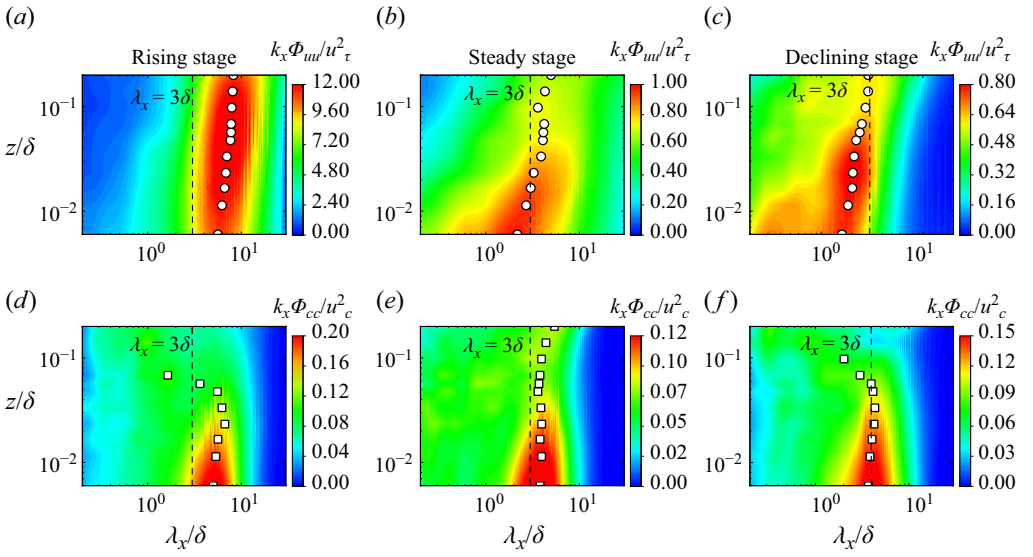


Figure 6. Colour contour maps of the variation in the one-dimensional premultiplied spectra with the wall-normal position during the sandstorm: (*a–c*) Streamwise velocity fluctuations and (*d–f*) dust concentration fluctuations, where (*a*) and (*d*) show the rising stage results, (*b*) and (*e*) show the steady stage results and (*c*) and (*f*) show the declining stage results. The white filled circle and square symbols denote the corresponding streamwise velocity and dust concentration premultiplied spectrum peaks, respectively.

are less than 3δ at the near ground and gradually increase with height, which is consistent with the laboratory and ASL results (Vallikivi *et al.* 2015; Wang & Zheng 2016). However, $(\lambda_{ux})_{max}$ are larger than 3δ at all heights in the rising stage, indicating that the VLSMs are already dominant feature in the flow field at the beginning of the sandstorm and exhibit global characteristics in the measurement range.The $(\lambda_{ux})_{max}$ are less than 3δ at all heights in the declining stage, indicating that VLSMs are difficult to maintain and gradually disappear due to decreasing wind velocity. The premultiplied spectra of the dust concentration fluctuations in the steady stage shown in figure 6(*e*) are similar to that of the streamwise velocity fluctuations shown in figure 6(*b*). The $(\lambda_{cx})_{max}$ also increase with height in the steady stage, but vary slightly across all z locations. Moreover, $(\lambda_{cx})_{max}$ are larger than $(\lambda_{ux})_{max}$ at the near ground and the difference decreases with increasing height, which is consistent with the difference of the streamwise extent of positive correlation region between velocity and dust concentration fluctuations. However, in the rising and declining stages, $(\lambda_{cx})_{max}$ rapidly decrease away from the ground (as shown in figure 6*d*,*f*), which significantly differs from the variation in $(\lambda_{cx})_{max}$ with height. A plausible explanation is that the low wind velocity during the rising and declining stages cannot be sufficient to transport dust particles to higher locations, resulting in a lack of dust particles needed to form the large-scale dust cluster structures, as shown by the instantaneous PM10 concentration (figure 3*d–f*).

4. Morphological characteristics of the large-scale two-phase structures during the sandstorm

The existence of large-scale turbulence/dust concentration coherent structures during the sandstorm is confirmed in § 3. The instantaneous velocity/dust concentration fluctuations,

https://doi.org/10.1017/jfm.2025.28 Published online by Cambridge University Press

two-point correlation contours and premultiplied spectra suggest that the two-phase structures exhibit significant morphological differences at the different stages of the sandstorm and from each other. This section presents a quantitative evolution of the morphological characteristics (streamwise length scale, structure inclination angle and self-similarity) of the two-phase structures during the sandstorm.

4.1. *Streamwise length scale*

The streamwise length scales are obtained from the one-dimensional correlations of the streamwise velocity fluctuations u and PM10 concentration fluctuations c for the constant spanwise and wall-normal positions, i.e.

$$R_{uu}(\triangle x) = \frac{\langle u(x,\, y,\, z)u(x+\triangle x,\, y,\, z)\rangle}{\sigma_{u(x,y,z)}\sigma_{u(x+\triangle x,y,z)}} \tag{4.1}$$

and

$$R_{cc}(\triangle x) = \frac{\langle c(x,\, y,\, z)c(x+\triangle x,\, y,\, z)\rangle}{\sigma_{c(x,y,z)}\sigma_{c(x+\triangle x,y,z)}} \tag{4.2}$$

where $\triangle x = U_c\triangle\tau$, U_c is the convection velocity and $\triangle\tau$ is the time lead and lag to satisfy the correlation. To extract the spatial scale from two-point correlation, a nominal threshold is necessary. A small positive threshold value not only effectively avoids the influence of background noise (Ganapathisubramani *et al.* 2006; Dennis & Nickels 2011), but also can maintain sufficiently accurate correlations to capture the spatial features of large-scale structures (Krogstad & Antonia 1994). Unfortunately, there are no standardized criteria for threshold selection. Zhou *et al.* (1999) suggested that the exact choice of threshold only affects the quantitative values but not the general vortex shape or the variation in the characteristic length. Therefore, a compromise threshold value of $R_{uu} = 0.2$ is selected in this study, which does not affect the results and conclusions.

The spatial and temporal variations in the streamwise length scale of the turbulence/dust concentration structures (denoted as L_{ux} and L_{cx}, respectively) during the sandstorm obtained by two-point correlation are shown in figure 7, where the qualitative evolution trends with time and height are given by red and green arrows, respectively. To compare the differences in the temporal evolution of L_{ux} and L_{cx}, the results at height $z/\delta = 0.03$ are plotted in figure 7(*c*). In the rising stage, L_{ux} (blue line) are large and slightly increase (from 1.5δ to 3.7δ) with initial increasing wind velocity, and then, with sandstorm development and the continuous increase in the wind velocity, L_{ux} gradually decrease. After full development, L_{ux} remain substantially invariant (approximately 1.6δ) in the steady stage, and the present results agree with the existing laboratory and ASL results within the experimental error range (as shown in figure 7*e*). When the sandstorm attenuates during the declining stage, L_{ux} decrease again. Namely, large-scale turbulence structures exist at the beginning of the sandstorm, but gradually decrease with sandstorm development in the rising stage, remain invariant during the steady stage and finally decrease with the attenuation of the sandstorm. In contrast, L_{cx} (yellow line) evolve from zero at the beginning of the sandstorm to gradually increasing with sandstorm development, reaching a plateau (approximately 4.3δ) in the steady stage, and then decreasing with a decrease in wind velocity until it decreases to zero at the end of the sandstorm. The differences in temporal evolution between two-phase structures are mainly in the rising stage, where dust concentration structures emerge gradually with sandstorm development, while turbulent large-scale structures are present from the beginning. Hence, the variations in L_{ux} and L_{cx} with wall-normal distance at different stage are given in figure 7(*d–f*). Throughout the entire sandstorm, the outer-scaled streamwise length scale

https://doi.org/10.1017/jfm.2025.28 Published online by Cambridge University Press

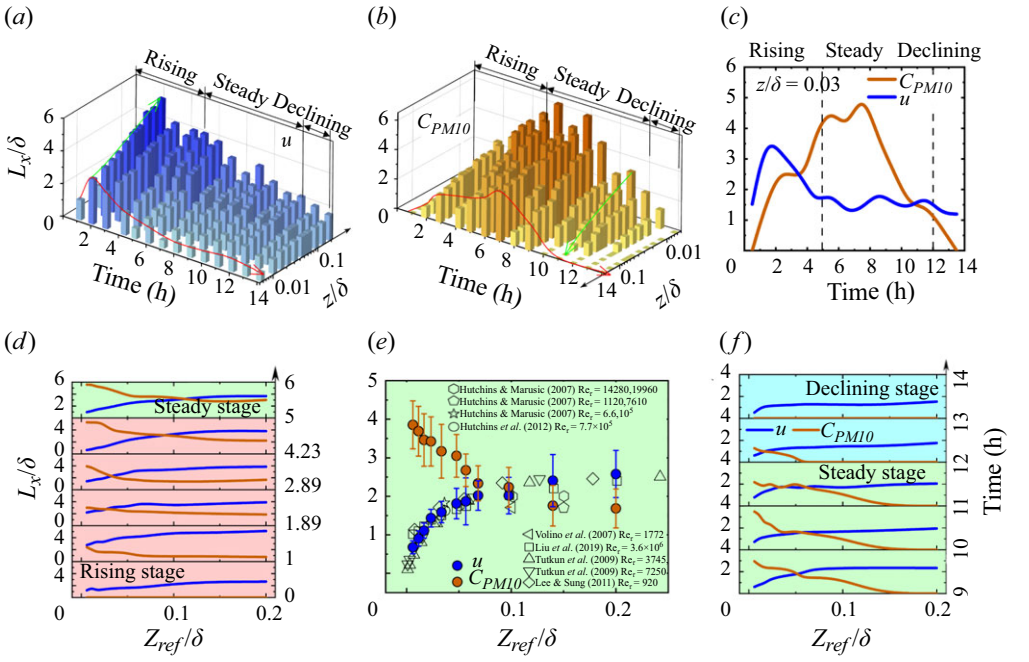


Figure 7. Spatial and temporal variations in the streamwise length scales of (*a*) the turbulence structures L_{ux} and (*b*) dust concentration structures L_{cx} during the sandstorm, where the red and green solid lines show the trends with time and wall-normal distance, respectively. (*c*) Evolution of L_{ux} and L_{cx} with time at a height $z/\delta = 0.03$, where the blue and yellow solid lines indicate the results of the streamwise velocity and dust concentration, respectively. (*d–f*) Comparison of the variations in L_{ux} and L_{cx} with wall-normal distance, where the light red, light green and cyan background represent the rising stage, steady stage and declining stage; the blue and yellow solid symbols denote L_{ux} and L_{cx}, respectively. (*e*) Average L_{ux} and L_{cx} in the steady stage, where hollow symbols are the existing laboratory and ASL results of L_{ux} (from Hutchins & Marusic 2007; Volino *et al.* 2007; Tutkun *et al.* 2009; Lee & Sung 2011; Hutchins *et al.* 2012; Liu *et al.* 2017*b*).

L_{ux}/δ is pronounced near the ground, and L_{ux}/δ appears to level off as the wake region is approached. Conversely, the variation trend of L_{cx}/δ is the mirror image of L_{ux}/δ and the difference with L_{ux}/δ decrease with height, as shown in figure 7(*d–f*). Moreover, L_{cx}/δ are less than L_{ux} at the beginning of the sandstorm, but as the sandstorm develops, L_{cx} gradually increase and exceed L_{ux} near the ground, as shown in figure 7(*d*). When the sandstorm reaches the steady stage with relatively constant wind velocity and dust concentration, L_{cx} at lower positions are greater than L_{ux}, the difference between L_{ux} and L_{cx} decreases with height, and the two are close at higher positions, but L_{ux} are slightly larger than L_{cx}, as shown in figure 7(*e*). Note that later in the steady stage, L_{ux} start to decrease before L_{ux}. In the declining stage, L_{cx} gradually decay to less than L_{ux} at all heights. Qualitative differences between the variations in two-phase structure scales along height suggest there are differences in their formation mechanisms. In addition, at the beginning and end of the sandstorm, L_{cx} equal zero at higher positions, indicating that the dust concentration structures originate from the ground and disappear at the positions far from the ground, as shown in figure 7(*d,f*). The streamwise time length scales obtained from the time autocorrelation are used to verify the streamwise spatial length scales obtained from the Taylor frozen hypothesis. The results show that the spatial and temporal evolution of the streamwise time length scales of turbulence/dust concentration structures is essentially the same as that of the streamwise spatial length scales, except that

https://doi.org/10.1017/jfm.2025.28 Published online by Cambridge University Press

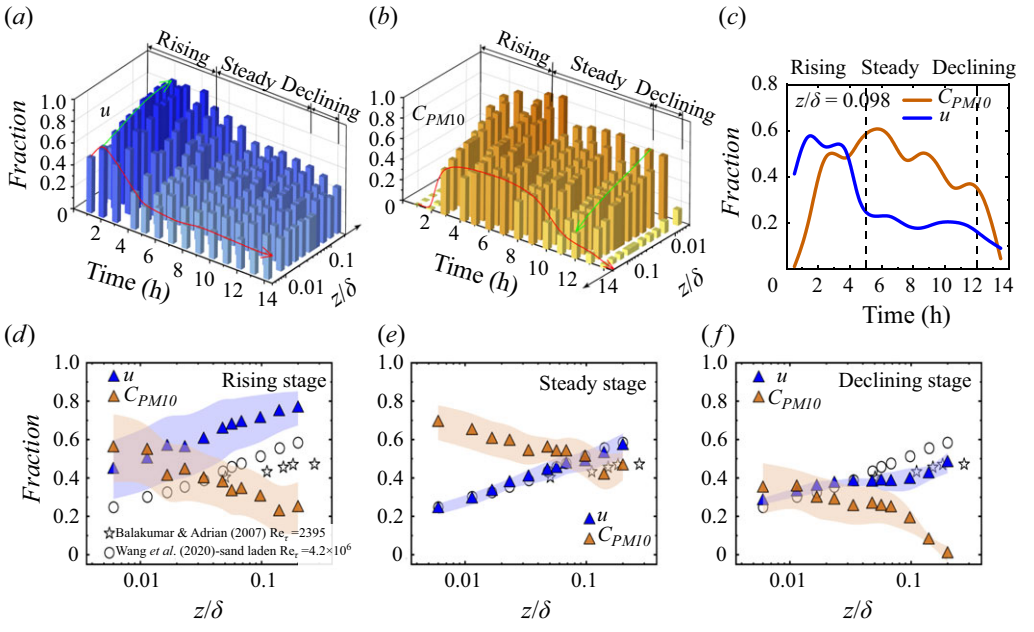


Figure 8. Same as figure 7 but for the fractional contribution of VLSMs to the total fluctuation intensity, where the black hollow star is the energy contribution of turbulence VLSMs given by Balakumar & Adrian (2007), and the hollow cycle is that of sand-laden flow at a similar Reynolds number in Wang *et al.* (2020).

the streamwise time length scales of the velocity structures show an increasing tendency at the end of sandstorms that is opposite to the streamwise spatial length scales. The increase in the streamwise time length scales of velocity structures in the declining is a result of the fact the vortex structures take longer to pass through the observed position due to the lower wind velocity. Furthermore, to analyse the fractional contribution of the very large-scale structures to the total fluctuation intensity of the streamwise velocity and dust concentration fluctuations during the sandstorm, the spatial and temporal evolution of the fractional contribution are also shown in figure 8. The evolutions of fractional contribution are qualitatively consistent with that at the streamwise length scale.

Changes in turbulence driving factors behind the sandstorms can provide a reasonable explanation for the evolutions of two-phase structures. With the intrusion of cold fronts, cold air masses encounter warmer local air, which causes convection, implying the beginning of sandstorm (Dragani 1999; Helfer & Nuijens 2021). The strong quadratic interaction causes synoptic-scale fluctuations to break into large-scale turbulence structures, being larger than the structures in the steady stage and moving downwards (Liu *et al.* 2022), referred to as the top-down mechanism, resulting in a gradual increase in L_{ux} with height, as shown in figure 7(*d*). Furthermore, at the initial rising stage, the wind velocity increases due to the energy carried by the cold air but the shear is small due to stronger atmospheric instability, resulting in the stretching of structures along the streamwise direction, namely, a short increase in L_{ux} at the initial rising stage, as shown in figure 7(*c*). With sandstorm development, the wind velocity increases and shearing breaking is enhanced, causing large-scale turbulence structures to be broken into smaller ones. Additionally, with enhanced wall shear, the hairpin vortices created by wall bursts are aligned coherently along the streamwise direction, forming larger-scale coherent structures, referred to as the bottom-up mechanism (Adrian *et al.* 2000). This can also lead

https://doi.org/10.1017/jfm.2025.28 Published online by Cambridge University Press

to increase in L_{ux} and fractional contribution of VLSMs with height. When these two mechanisms are combined, L_{ux} and fractional contribution of VLSMs are significant. The maximum contribution can reach up to 75 % at approximately the top of the logarithmic region in the rising stage, as shown in figure 8(*d*), which is much larger than results reported in previous document (the maximum at the same location is 60 %(Wang & Zheng 2016)).

When the cold air completely occupies the observation area, the flow is dominated by shear turbulence (Liu *et al.* 2022). The large-scale turbulence structures mainly originate from the self-organization process of the hairpin vortices (Balakumar & Adrian 2007; Vallikivi *et al.* 2015). The streamwise length scale and the fractional contributions of the large-scale turbulence structures increase with height and present results in the steady stage are consistent with existing laboratory and ASL results (Balakumar & Adrian 2007; Hutchins & Marusic 2007; Volino *et al.* 2007; Tutkun *et al.* 2009; Lee & Sung 2011; Hutchins *et al.* 2012; Liu *et al.* 2017*b*; Wang *et al.* 2020), as shown in figures 7(*e*) and 8(*e*), respectively. In the declining stage, with the end of the cold front transit event, the exhausted energy brought by the cold air mass leads to a decreasing wind velocity, making it challenging to sustain large-scale structures. Therefore, the large-scale turbulence structures gradually dissipate and energy gradually concentrates towards small-scale motions with the attenuation of the sandstorm.

The large-scale turbulence structures significantly contribute to the transport of dust particles and influence the distribution of dust particles in the flow field (Maxey 1987; Balachandar & Eaton 2010; Marusic *et al.* 2010). Consequently, the changes in the turbulence structures cause differences in the dust concentration structures at the different stages. At the beginning of the sandstorm, the wind velocity is low and the main driving factor is buoyancy-driven thermal turbulence (Liu *et al.* 2024), implying that dust particles cannot be released from the ground and carried into the air (Lim & Chun 2006; Niu *et al.* 2012; Mockford *et al.* 2018). Additionally, the upstream dust particles have not yet reached the observation area. Therefore, there are no dust cluster structures, as shown in figure 7(*b–d*). With sandstorm development, the dust particles are released from sandy surfaces by enhanced shear turbulence and transported upward by ejections-Q2-type events (Marchioli & Soldati 2002; Zhang *et al.* 2018). That is, dust concentration structures are organized from the ground surface, evolving towards higher atmospheric layer. The streamwise extent of high-concentration regions formed by dust clusters, i.e. L_{cx} become larger with increasing wind velocity and dust concentration, as shown in figure 7(*c*). Moreover, as a number of large-scale dust concentration structures generate, their fractional contribution gradually increases, as shown in figure 8(*c*). When shear turbulence becomes dominant in the steady stage, sufficient dust particles form large-scale dust structures under the high-strain effect contributed by the turbulence structures, and these very large-scale dust concentration structures are dominant in dust concentration field and contribution to the total fluctuation intensity reaches 70 % near the ground, as shown in figures 7(*e*) and 8(*e*). This is different from the case of turbulence, where the energy contribution of VLSMs is strongest in the rising stage. In the declining stage, the atmosphere turns into a stable stratification, inhibiting the atmospheric turbulence and its diffusion (Chauhan *et al.* 2013; Liu *et al.* 2017*a*). The weakened shear is insufficient to lift enough dust particles from the ground and these dust particles cannot be transported to higher positions, thus their activity is limited to the near-ground region. As a result, the scales of dust structures gradually decrease with continuously decreasing wind velocity and large-scale dust structures cannot form away from the ground, as shown in figure 7(*f*).

Although dust particles exhibit a great capability to follow eddies, the observed decrease in L_{cx} with height, in contrast to the behaviour of L_{ux}, reveals a qualitative

https://doi.org/10.1017/jfm.2025.28 Published online by Cambridge University Press

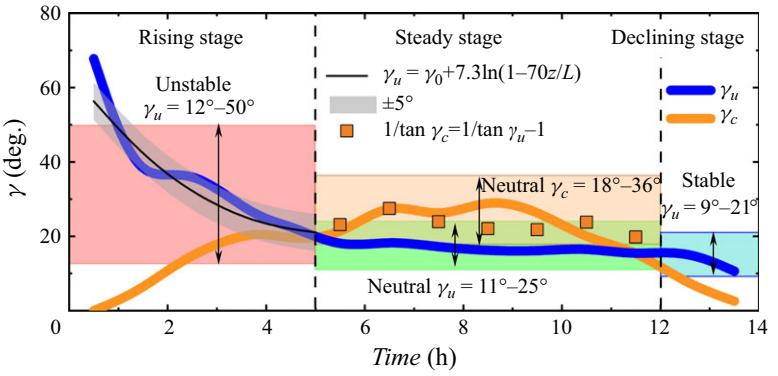


Figure 9. Evolution of structure inclination angle of the turbulence structures (γ_u, blue line) and dust concentration structures (γ_c, yellow line). The light red, green and blue areas denote the ranges of turbulence structure inclination angle γ_u in unstable, neutral and stable surface layers from Hommema & Adrian (2003); Morris *et al.* (2007); Marusic & Heuer (2007); Hutchins *et al.* (2012); Chauhan *et al.* (2013); Liu *et al.* (2017*a*) and He & Liu (2023). The light yellow area denotes the range of the dust concentration structure inclination angle γ_c given by He & Liu (2023). The black solid line in the rising stage denotes the turbulence structure inclination angle γ_u calculated by the empirical model $\gamma_u = \gamma_0 + 7.3\ln(1 - 70z/L)$ (where γ_0 is the inclination angle in the neutral regime) from Chauhan *et al.* (2013). The yellow filled squares in the steady stage denote the dust concentration structure inclination angles γ_c calculated by the relationship model ($1/\tan\gamma_c = 1/\tan\gamma_u - 1$) given by He & Liu (2023).

distinction between the two-phase structures. The interpretation could be that as the dust concentration decreases with height, the large-scale dust concentration structures cannot maintain coherence due to a lower concentration at a higher position and more small-scale structures are created, resulting in a decreasing scale with height. Additionally, larger dust particles near the ground have a larger time scale and filter out the effects of the smaller fluid scales (Marchioli & Soldati 2002), resulting in a lower correlation magnitude with velocity fluctuations than that of the dust concentration fluctuations (He & Liu 2023). Moreover, the follow ability of particles increases with decreasing average particle size ($d = 10$ μm at $z/\delta = 0.006$, while $d = 7$ μm at $z/\delta = 0.2$). Therefore, the difference between L_{ux} and L_{cx} decrease with height, as shown in figure 7(*e*). Additionally, the evolution of the fractional contribution of very large-scale fluctuations to the total fluctuation intensity in figure 8 provides further evidence supporting for the origin of two-phase coherent structures.

4.2. *Structure inclination angle*

In the near-neutral flow, coherent structures have been associated with characteristic inclination angles because of the mean shear (Liu *et al.* 2017*a*). However, the buoyancy effect, addition of sand particles and flow acceleration inherent in the sandstorm process could influence the inclination angle. Consequently, the evolution of two-phase structure inclination angles (denoted as γ_u and γ_c, respectively) throughout the sandstorm process is shown in figure 9. In this study, the average structure inclination angle is obtained from the two-point correlations of the lowest signal with signals at higher wall-normal positions,

$$\gamma = \arctan\left(\left\langle \triangle z/\triangle x^* \right\rangle\right) = \arctan\left(\left\langle \triangle z/\left(U_c \triangle t^*\right)\right\rangle\right), \tag{4.3}$$

where $\triangle x^* = U_c \triangle t^*$ and $\triangle t^*$ are the spatial and time delay of the peak locations of R_{uu} or R_{cc} obtained from (3.2) and (3.3).

https://doi.org/10.1017/jfm.2025.28 Published online by Cambridge University Press

It is seen that γ_u gradually decrease with the development of the sandstorm. At the beginning of the sandstorm, γ_u reaches 68°. With sandstorm development, γ_u gradually decrease and basically fall within the range given by the existing studies under unstable conditions (12°–50°, as shown by the light red area). Considering that the buoyancy effect could lead the head of coherent structures to be lifted up from the ground and become steeper (Chauhan *et al.* 2013; Salesky & Anderson 2018), γ_u calculated by an empirical model ($\gamma_u = \gamma_0 + 7.3\ln(1 - 70z/L)$, where γ_0 is the inclination angle in the neutral regime (Chauhan *et al.* 2013), are also included (marked by the black solid line in the rising stage) for comparison. The general trend of the present results agrees well with the empirical model, except in the initial stages. In the early stages of the sandstorm, the low wind velocity and the small velocity gradient under the unstable condition are not sufficient to allow turbulence structures to tilt substantially along the wall-normal direction. Moreover, strong buoyancy effect leads to a significant lifting on the structures. Thus, there is a large γ_u. As sandstorm develops and wind velocity increases, on the one hand, the shear turbulence is enhanced and hairpin vortex packets are stretched by the velocity gradient of the streamwise wind velocity in the wall-normal direction, making the large-scale structures have a certain tilt angle with the ground (14° according to the hairpin vortex packet model in Adrian *et al.* (2000); on the other hand, the velocity gradient along the wall-normal direction increases with decreasing atmospheric instability, resulting in decreasing γ_u because γ_u is inversely proportional to the velocity gradient (Liu *et al.* 2017*a*; Lotfy & Harun 2018). Additionally, the flow acceleration induces an increase in Reynolds shear stresses in the near-wall region (Talamelli *et al.* 2002), which consequently contributes to a potential reduction in γ_u due to its negative correlation with wall shear (Liu *et al.* 2017*a*). Nevertheless, the present results suggest that the effect of flow acceleration on γ_u appears to be negligible when compared with the influence of thermal instability.

When the sandstorm develops into the steady stage, γ_u remain essentially invariant at approximately 16.63°. Although this value falls within the range of 11° to 25° given by near-neutral laboratory and ASL studies (as shown by the light green area), it is larger than the results of the near-neutral particle-free ASL (e.g. $\gamma_u = 13.7°$, Chauhan *et al.* (2013) and $\gamma_u = 13.02°$, Liu *et al.* (2017*a*)). This is consistent with the observations of Tay *et al.* (2015) and He & Liu (2023) in the particle-laden flows, where the addition of sand particles causes an increase in γ_u. In the declining stage, γ_u are in agreement with the range (9°–12°, as shown by the light blue area) given by existing studies in stable condition but decrease with the attenuation of the sandstorm. When the atmosphere transforms into stable stratification, suppressing effect of the sinking cold and denser air results in a decrease in structure inclination angle (Chauhan *et al.* 2013; Liu *et al.* 2017*a*).

In stark contrast to the behaviour of γ_u, γ_c equals zero in the initial stage of the sandstorm and then γ_c gradually increase and approach γ_u with sandstorm development in the rising stage, which is similar to the evolutionary pattern of streamwise length scale L_{cx}. This suggests that dust particles form flat and small structures early in the sandstorm. As shear turbulence enhances, more and more dust particles are captured by the turbulence structures and transported upwards, forming dust structures. Their inclination gradually exceed that of the turbulence structures. In the steady stage, γ_c reach a plateau that is larger than γ_u. This phenomenon is primarily attributed to the fact that the heavier particles near the ground tend to cross the path of the fluid flow and accumulate in the region of high strain and low vorticity (Maxey 1987; Eaton & Fessler 1994; Wang *et al.* 2024), causing a particle–turbulence structure phase difference that varies with height (He & Liu 2023), which culminates in γ_c larger than γ_c in the steady stage. The γ_c obtained from the relationship model ($1/\tan\gamma_c = 1/\tan\gamma_u - 1$) given by He & Liu (2023) are marked by yellow filled square symbols in figure 9. It is observed that, in the steady stage, γ_c not

https://doi.org/10.1017/jfm.2025.28 Published online by Cambridge University Press

only fall within the range given by He & Liu (2023), but also satisfy the relationship. In the stable declining stage, the suppressing effect also acts on the dust concentration structures, resulting in a decrease in γ_c until it becomes zero at the end of sandstorm. Notably, in the middle and late stages of the sandstorm, γ_c decreases earlier than γ_u, echoing the L_{cx} decreases earlier than L_{ux}, which indicates that stable stratification has a stronger suppressing effect on dust transport than on turbulence.

4.3. *Self-similarity*

To inspect the self-similarity and assess the wall-attached aspect, the LCS is adopted as a statistical tool for effectively detecting self-similar eddies (Baars *et al.* 2017; Baidya *et al.* 2019; Krug *et al.* 2019; He & Liu 2023). The LCS defined as

$$\gamma^2_{\mathrm{LCS}}\left(z, z_{ref}, \lambda_x\right) = \frac{\left|\left\langle \tilde{u}\left(z;\lambda_x\right)\overline{\tilde{u}^*\left(z_{ref};\lambda_x\right)}\right\rangle\right|^2}{\left\langle\left|\tilde{u}\left(z;\lambda_x\right)\right|^2\right\rangle\left\langle\left|\tilde{u}\left(z_{ref};\lambda_x\right)\right|^2\right\rangle} = \frac{\left|\Phi_{uu}\left(z, z_{ref};\lambda_x\right)\right|^2}{\Phi_{uu}\left(z;\lambda_x\right)\Phi\left(z_{ref};\lambda_x\right)}, \quad (4.4)$$

where z_{ref} and z are the spatial measurement heights for the reference and traversing position; $\tilde{u}^*(z;\lambda_x)$ is the Fourier transform of velocity fluctuation $u(z)$, λ_x is the streamwise wavelength, the asterisk $*$ denotes the complex conjugate, $|\ |$ designates the modulus and $<>$ denotes ensemble averaging. Moreover, $\Phi_{uu}(z, z_{ref};\lambda_x)$ and $\Phi_{uu}(z;\lambda_x)$ are the cross-spectrum and power spectral spectrum, respectively. The LCS is the square of a scale-specific correlation coefficient and can assess the linear coherence between the velocity fluctuations u of each scale (Baars *et al.* 2017). According to the definition $0 \le \gamma^2_{LCS} \le 1$, $\gamma^2_{LCS} = 0$ indicates that the scale is not correlated and $\gamma^2_{LCS} = 1$ denotes perfect. This coherence can also be estimated across all other measured signals, such as spanwise velocity, temperature (Krug *et al.* 2019) and dust concentration fluctuations (He *et al.* 2024).

The γ^2_{LCS} spectra of streamwise velocity fluctuations u and dust concentration fluctuation C_{PM10} are shown as a coherence spectrogram in figures 10(*a–c*) and 10(*d–f*) , respectively. As seen, the isocontour map of $\gamma^2_{LCS}(z, z_{ref};\lambda_x)$ is a function of λ_x and $\triangle z$ ($\triangle z = z - z_{ref}$ is the distance between the reference and traversing positions). The reference height $z_{ref} = 0.006\delta$ is adopted in this study. It should be noted that a lower reference position allows for better capture of the wall-attached hierarchical organization of eddies, but it is still difficult to measure very close to the ground in field observations. For a large value of $\triangle z$ ($z \gg z_{ref}$,), there is no obvious difference between plotting γ^2_{LCS} as a function of z and $\triangle z$ (Krug *et al.* 2019; He *et al.* 2024). Therefore, in this study, normalization with $\triangle z$ is employed, as this provides a more extensive scaling region. Following the conceptual model of γ^2_{LCS} isocontours conducted by Baars *et al.* (2017), when they superpose each hierarchy of self-similar scales, the coherence contours are additive, implying that there exists a triangular region in the $(\lambda_x, \triangle z)$-space where the isocontours of γ^2_{LCS} align with lines of constant $\lambda_x/\triangle z$ (as shown by the red dashed line). These regions can be obviously observed in figures 10(*b*), 10(*c*) and 10(*e*), indicating that the velocity and dust concentration fluctuations at the steady stage and the velocity fluctuations at the declining stages may contain self-similar wall-attached structures. The geometrical self-similar wall-attached structures indicate that the value of γ^2_{LCS} linearly increases with $\log(\lambda_x)$ at a constant height z and decreases with $\log(z)$ for a constant streamwise wavelength λ_x in the self-similar region. The region adheres to

$$\gamma^2_{LCS} = C_1 \ln\left(\lambda_x/\triangle z\right) + C_2, \quad (4.5)$$

https://doi.org/10.1017/jfm.2025.28 Published online by Cambridge University Press

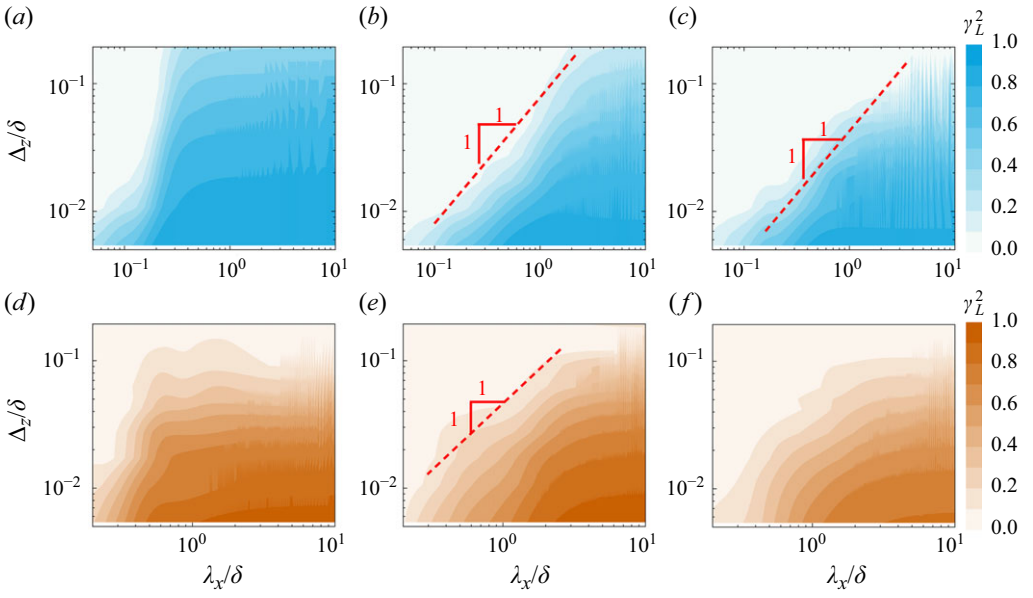


Figure 10. Coherence spectrogram of streamwise velocity fluctuations u (*a–c*) and dust concentration fluctuations C_{PM10} (*d–f*) in the different stages of the sandstorm, where (*a*) and (*d*) is the rising stage, (*b*) and (*e*) is the steady stage and (*c*) and (*f*) is the declining stage.

where C_1 and C_2 are constants. The statistical aspect ratio (streamwise/wall-normal) then follows

$$AR = \frac{\lambda_x}{\triangle z}\,|_{\gamma^2_{LCS}} = \exp\left(-\frac{C_2}{C_1}\right). \tag{4.6}$$

The γ^2_{LCS} spectra of figure 10 can be presented as a function of $\lambda_x/\triangle z$, as shown in figure 11. As expected, within the self-similar region, all LCSs collapse. By inspection, in the flow field, the completely separated LCS lines at the different heights in the rising stage (as shown in figure 11*a*) imply that the turbulence structures do not satisfy self-similarity. However, all LCS lines collapse well in a certain wavelength range in the steady stage (as shown in figure 11*b*), indicating that these turbulence structures exhibit self-similarity as described by the attached eddy model. As shown in figure 11(*c*), in the declining stage, the coherence at the higher positions attenuates to a very low level, but there is still a region with collapsed LCS lines near the ground, indicating that the self-similarity is satisfied in the near-ground under weakly stable stratification. For the dust concentration fluctuations, collapsed LCS lines can be observed in figure 11(*e*) but are absent in figure 11(*d*,*f*), indicating that wall-attached self-similar dust cluster structures only occur in the steady stage. Identifying the scaling region by the range of this collapse (marked in red in the figure) allows us to fit (4.5) and (4.6) to the data and to extract the statistical aspect ratio, as shown by the grey solid line in figure 11(*b*,*c*,*e*).

The observed self-similarity indicates that the LCS lines at different heights follow the same increasing pattern with increasing wavelength; that is, the aspect ratio remains invariant across different the heights. The evolution of the aspect ratio of the streamwise velocity fluctuations (AR_u) and the dust concentration fluctuation (AR_c) at the different heights during the sandstorm are plotted in figure 12. Notably, the self-similarity region gradually decreases with height because only larger hierarchies can be captured when

https://doi.org/10.1017/jfm.2025.28 Published online by Cambridge University Press

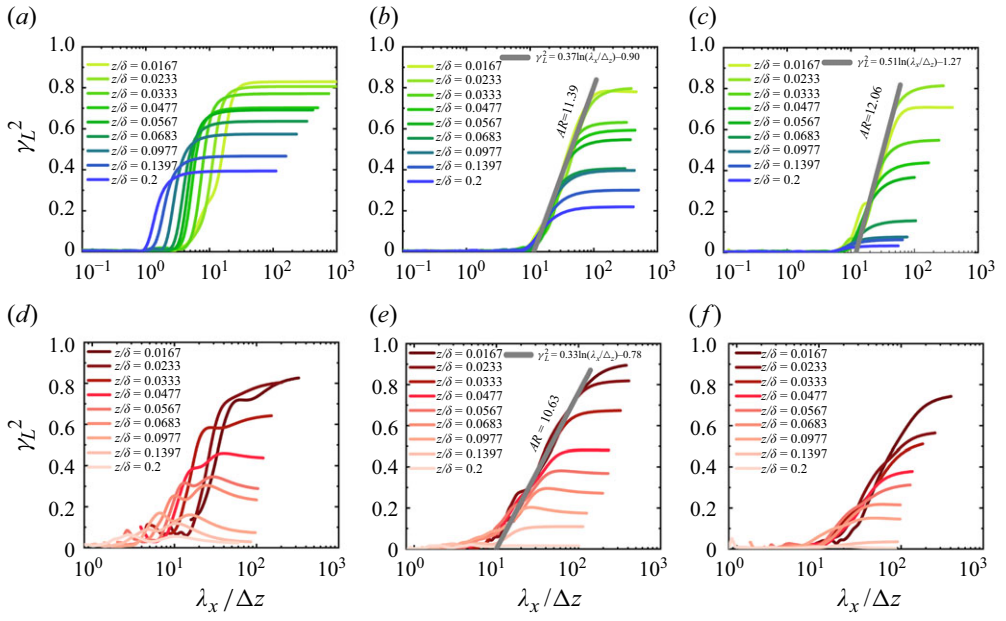


Figure 11. Obtained LCSs are plotted as a function of $\lambda_x/\Delta z$. The layout is the same as in figure 10.

the traversing points become higher, which leads to a significant error in the aspect ratios obtained by fitting, thus the results for the two positions farthest away from the reference positions are not shown in figure 12. In particular, the relative contributions at high λ_x, as well as farther away from the ground, are considerably lower for the C_{PM10} spectrogram compared with the streamwise velocity, which is consistent with the temperature fluctuation (Krug *et al.* 2019). Additionally, AR_c at the beginning and end of the sandstorm are not considered in figure 12(*b*) because the dust concentration levels at this point are low enough to form significant dust clusters structures.

As expected, AR_u remain essentially invariant with height in the steady stage, elucidating the self-similarity of turbulence coherent structures. This is readily explicable because the turbulence structures in the steady stage mainly originate from the self-organization process of the hairpin vortices (Baars *et al.* 2017; Marusic & Monty 2019). The present result $AR_u = 12.19$ agrees with the particle–laden flow result ($AR_u = 12.8$, He *et al.* 2024) but is smaller than the particle-free flow results ($AR_u = 14$, Baars *et al.* (2017); $AR_u = 13.9$, Duan *et al.* (2020); $AR_u = 14.1$, He *et al.* (2024)), as shown in figure 12(*a*). In contrast to the steady stage, AR_u gradually increases with the sandstorm development at the rising stage, but decreases with height, indicating that self-similarity is not satisfied. The general trend in present AR_u in the rising stage follows the empirical equation ($AR_u = -3.1\log_{10}(-z/L) + 3.0$, as marked by the red square (Krug *et al.* 2019)), i.e. AR_u increase with the weakening stratification instability. However, the AR_u at different heights cannot be qualified by this equation. Note that the rising stage is characterized by sharp flow acceleration in addition to the changes in thermal stability. The flow acceleration significantly enhances the near-wall Reynolds shear stresses (Fernholz & Warnack 1998; Piomelli *et al.* 2000), making the large-scale coherent structures more elongated near the ground (Talamelli *et al.* 2002). Consequently, the turbulence structures near the ground in the rising stage exhibit a larger aspect ratio; that is, AR_u decreases with height. In the declining stage, AR_u are relatively invariant near the ground, but decrease at

https://doi.org/10.1017/jfm.2025.28 Published online by Cambridge University Press

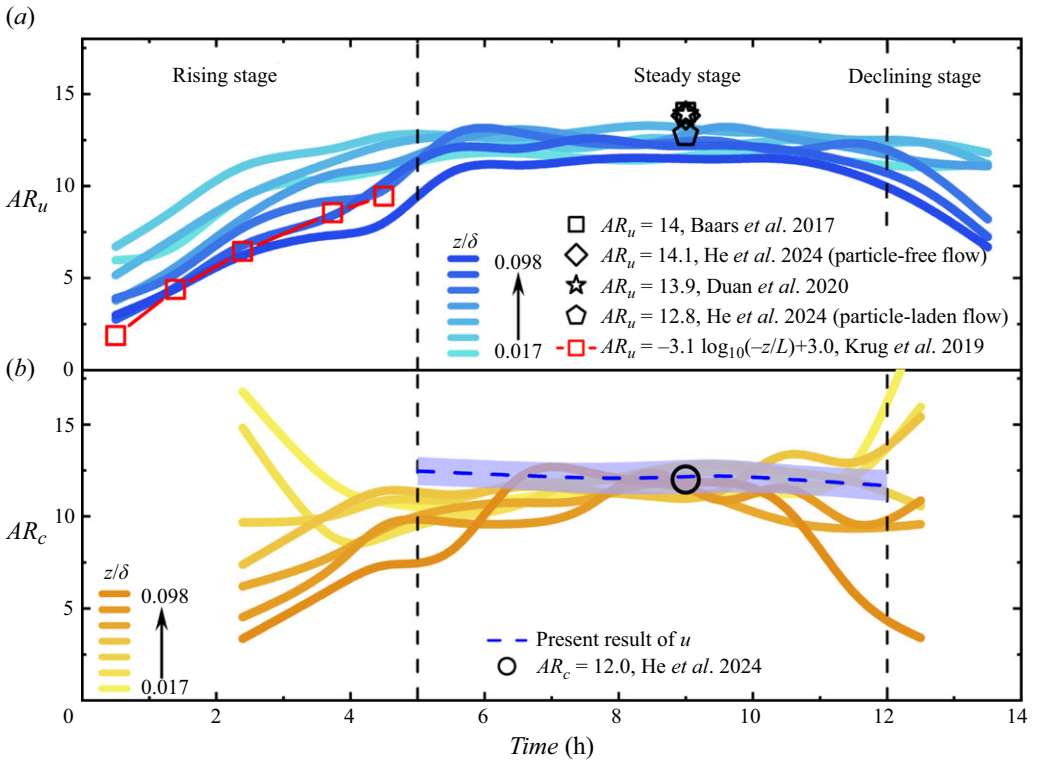


Figure 12. Evolution of aspect ratios at different heights during the sandstorm: (*a*) streamwise velocity fluctuation u (denotes AR_u); (*b*) dust concentration fluctuation C_{PM10} (denotes AR_c). The black hollow symbols denote the existing laboratory and ASL data (from Baars *et al.* 2017; Krug *et al.* 2019; Duan *et al.* 2020; He *et al.* 2024) and the red square denotes the result of the empirical formula from Krug *et al.* (2019). The blue dashed line denotes the present aspect ratio of the streamwise fluctuation u.

higher positions. This trend can be attributed to the attenuated shear turbulence, especially suppressed by gravity when stably stratified, results in a scale reduction and self-similar wall-attached structures cannot extend to the highest measured position (approximately 0.2δ) (Chauhan *et al.* 2010,2013; Liu & Zheng 2024). Namely, the turbulence structures adhere to self-similarity near the ground but are not satisfied at higher positions under the weak stable stratification because there is no longer a coherent region at higher positions.

Figure 12(*b*) suggests that the dust structures exhibit self-similarity in the steady stage, as evidenced by the independence of AR_c on the height, which is similar to the behaviour of turbulence structures. The present aspect ratio $AR_c = 11.39$ is close to $AR_c = 12.0$ reported by He *et al.* (2024). Dust particles with great capability to follow eddies in the flow are entrapped by wall-attached turbulence structures with low momentum, and cluster with each other in the low-speed regions, evolving with them in a self-similar way (Zhu *et al.* 2021). This indicates that the self-similarity of dust structures arises from the self-similarity of multiscale turbulence structures (Monchaux *et al.* 2010; Baker *et al.* 2017; Zhu *et al.* 2021). However, statistical $AR_c = 11.39$ is smaller than $AR_u = 12.19$ in the steady stage. Comparing the definitions of inclination and aspect ratio, the decrease of the aspect ratio can be anticipated by the increase of inclination. Dust structures are not self-similar in the rising and declining stages, which is expected because the self-similarity of turbulent structures is absent in the entire measured region. Moreover, akin to AR_u, AR_c decreases with height. Nevertheless, there is a distinctive difference between AR_c

https://doi.org/10.1017/jfm.2025.28 Published online by Cambridge University Press

and AR_u near the ground, where AR_c is not only significantly larger than AR_u, but also evolves with time in the opposite way to AR_u.

5. Conclusion

The evolution of the morphological characteristics of turbulence/dust concentration structures has been originally investigated based on the high-frequency synchronous multipoint measurement of multiphysics at QLOA during an entire sandstorm process. Dust concentration structures are observed at different sandstorm stages, which are similar to the turbulence structures. These two-phase structures adhere to self-similarity in the steady stage, but fail in the non-stationary stage. This is mainly attributed to the strong flow acceleration in the rising stage, which significantly elongates structures near the ground, and the suppression effect in the stable declining stage, which reduces the structure scales at higher positions. However, the evolution of dust structures is not analogous to that of turbulence structures, exhibiting distinct patterns.

The large-scale turbulence structures already exist and exhibit persistent spatial extension at the beginning of the sandstorm. These structures tilt significantly due to small shear and significant buoyancy effect under unstable conditions. Initially there is a period of slight increase in turbulence structure scales due to increasing velocity but small shear. As the sandstorm evolves, the enhanced shear breaks large-scale turbulence structures into smaller ones. Their scales and inclination angles decrease with weakening stratification instability, and then remain invariant in the steady stage. However, the evolution of the dust concentration structures does not follow the trends observed in turbulence structures, exhibiting distinct ones. Their morphology exhibits a ridge-like evolutionary trend, i.e. dust concentration structures gradually appear in the rising stage and the scales and inclination angles increase until they reach a maximum in the steady stage, being larger and steeper than the turbulence structures, and then begin to decrease. In the declining stage, the sinking cold air and denser air inhibit atmospheric turbulence and diffusion, resulting in a decrease in the scale and inclination angle of two-phase structures, but the dust structures decay more rapidly.

Throughout the entire sandstorm, the turbulence structure scales increase with height, while dust concentration structure scales exhibit a converse trend because the decrease in dust concentration with height results in large-scale dust concentration structures which cannot maintain their coherence at higher positions and more small-scale structures are created. Moreover, dust concentration structure scales are larger than turbulence structure scales near the ground due to the poor response of larger dust particles to small-scale turbulence fluctuations. However, the decreasing particle diameter with height leads to an increasing follow ability of dust particles, thus the scale difference in two-phase structure decreases with height. Furthermore, the variation of particle diameter with height also imparted to the dust structures have a larger inclination and a smaller aspect ratio than turbulence structures.

Funding. This study was supported by grants from the National Natural Science Foundation of China (12388101, 92052202 and 12372217). The authors would like to express their sincere appreciation for the support.

Declaration of interests. The authors report no conflict of interest.

Appendix A. Results of the streamwise time length scale of the two-phase structure

In this appendix, we present the results of the streamwise time length scale of the two-phase structure to verify the conclusions of the streamwise spatial length scale L_x.

https://doi.org/10.1017/jfm.2025.28 Published online by Cambridge University Press

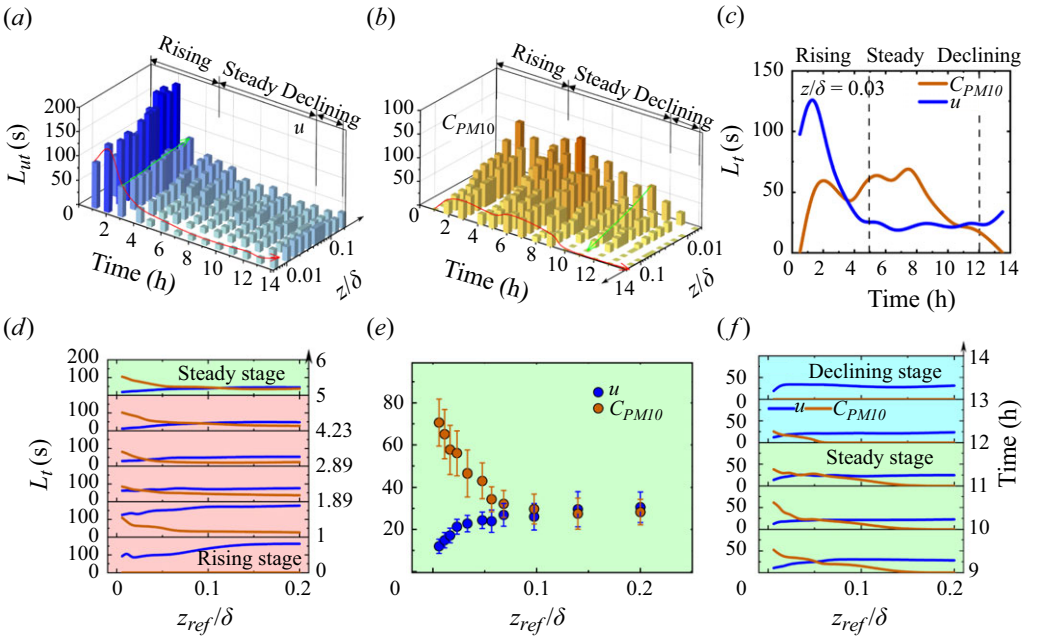


Figure 13. Spatial and temporal variations in the streamwise length scales of (*a*) the turbulence structures L_{ut} and (*b*) dust concentration structures L_{ct} during the sandstorm, where the red and green solid lines show the trends with time and wall-normal distance, respectively. (*c*) Evolution of L_{ut} and L_{ct} with time at a height $z/\delta = 0.03$, where the blue and yellow solid lines indicate the results of the streamwise velocity and dust concentration, respectively. (*d–f*) Comparison of the variations in L_{ut} and L_{ct} with wall-normal distance, where the light red, light green and cyan background represent the rising stage, steady stage and declining stage; the blue and yellow solid symbols denote L_{ut} and L_{ct}, respectively. (*e*) Average L_{ut} and L_{ct} in the steady stage.

The spatial and temporal variations in the streamwise time length scale of the turbulence/dust concentration structures (denoted as L_{ut} and L_{ct}, respectively) during the sandstorm obtained by two-point correlation are shown in figure 13, where the blue markers are the results of velocity fluctuating and the yellow markers are the results of dust concentrations fluctuating. The evolution of the streamwise time length scale L_{ut} of the streamwise velocity fluctuating in the rising and steady stages is similar to that of the streamwise spatial length scale L_{ux}, i.e. L_{ut} experiences a slight increase at the beginning of the rising stage, then, with sandstorm development and the continuous increase in the wind velocity, L_{ut} gradually decrease, and L_{ut} remain substantially invariant in the steady stage. In the declining stage, L_{ut} and L_{ux} evolve quite differently, i.e. L_{ut} show an increasing trend. This is because although shear flow is suppressed by the stable stratification during the declining stage, there is still shear to form small coherent structures. The lower wind velocity in the declining stage implies that these structures take longer to pass through the observed position. The streamwise time length scale of dust concentration structures is qualitatively similar to its spatial length scale evolution throughout the sandstorm. Namely, L_{ct} evolve from zero at the beginning of the sandstorm to gradually increasing with sandstorm development, reaching a plateau in the steady stage, and then decreasing with decreasing in wind velocity until it decreases to zero at the end of the sandstorm. As shown in figure 13(*d–f*), the variations in streamwise time length scale with wall-normal distance at different stage is essentially the same as that of the spatial scale.

https://doi.org/10.1017/jfm.2025.28 Published online by Cambridge University Press

References

Adrian, R.J., Meinhart, C.D. & Tomkins, C.D. 2000 Vortex organization in the outer region of the turbulent boundary layer. *J. Fluid Mech.* **422**, 1–54.

Baars, W.J., Hutchins, N. & Marusic, I. 2017 Self-similarity of wall-attached turbulence in boundary layers. *J. Fluid Mech.* **823**, R2.

Baidya, R. et al. 2019 Simultaneous skin friction and velocity measurements in high Reynolds number pipe and boundary layer flows. *J. Fluid Mech.* **871**, 377–400.

Baidya, R., Philip, J., Hutchins, N., Monty, J.P. & Marusic, I. 2017 Distance-from-the-wall scaling of turbulent motions in wall-bounded flows. *Phys. Fluids* **29** (2), 020712.

Bailey, S.C. & Smits, A.J. 2010 Experimental investigation of the structure of large- and very-large-scale motions in turbulent pipe flow. *J. Fluid Mech.* **651**, 339–356.

Baker, L., Frankel, A., Mani, A. & Coletti, F. 2017 Coherent clusters of inertial particles in homogeneous turbulence. *J. Fluid Mech.* **833**, 364–398.

Balachandar, S. & Eaton, J.K. 2010 Turbulent dispersed multiphase flow. *Annu. Rev. Fluid Mech.* **42** (1), 111–133.

Balakumar, B.J. & Adrian, R.J. 2007 Large- and very-large-scale motions in channel and boundary-layer flows. *Philos. Trans. R. Soc. A Math. Phys. Engng Sci.* **365** (1852), 665–681.

Baltzer, J.R., Adrian, R.J. & Wu, X. 2013 Structural organization of large and very large scales in turbulent pipe flow simulation. *J. Fluid Mech.* **720**, 236–279.

Barenblatt, G.I. & Golitsyn, G.S. 1974 Local structure of mature dust storms. *J. Atmos. Sci.* **31** (7), 1917–1933.

Behrooz, R.D., Kaveh, M., Parya, B., Panagiotis, G., Hamid, K., G, , Dimitris, G. & K 2022 Long-term (2012–2020) PM10 concentrations and increasing trends in the Sistan Basin: the role of levar wind and synoptic meteorology. *Atmos. Pollut. Res.* **13** (7), 101460.

Bernardini, M., Pirozzoli, S. & Orlandi, P. 2013 The effect of large-scale turbulent structures on particle dispersion in wall-bounded flows. *Intl J. Multiphase Flow* **51**, 55–64.

Brown, G.L. & Thomas, A.S.W. 1977 Large structure in a turbulent boundary layer. *Phys. Fluids* **20** (10), S243–S252.

Carper, M. & Porté-Agel, F. 2004 The role of coherent structures in subfilter-scale dissipation of turbulence measured in the atmospheric surface layer. *J. Turbul.* **500**, N40.

Chauhan, K., Hutchins, N., Marusic, I. & Monty, J. 2010 Two-point correlation statistics in the atmospheric surface layer. In *Proceedings of 17th Australasian Fluid Mech Conference Paper*, Auckland, New Zealand.

Chauhan, K., Hutchins, N., Monty, J. & Marusic, I. 2013 Structure inclination angles in the convective atmospheric surface layer. *Boundary-Layer Meteorol.* **147** (1), 41–50.

Choobari, O.A., Zawar-Reza, P. & Sturman, A. 2012 Atmospheric forcing of the three-dimensional distribution of dust particles over Australia: a case study. *J. Geophys. Res. Atmos.* **117** (D11), D11206.

Christensen, K.T. & Adrian, R.J. 2001 Statistical evidence of hairpin vortex packets in wall turbulence. *J. Fluid Mech.* **431**, 433–443.

Corrsin, S. & Kistler, A. 1955 Free-stream boundaries of turbulent flows, Report NACA-TR-1244. N.A.C.A. Technical Note.

Dennis, D.J.C. & Nickels, T.B. 2011 Experimental measurement of large-scale three-dimensional structures in a turbulent boundary layer. Part 1. Vortex packets. *J. Fluid Mech.* **673**, 180–217.

Dragani, W.C. 1999 A feature model of surface pressure and wind fields associated with the passage of atmospheric cold fronts. *Comput. Geosci.* **25** (10), 1149–1157.

Duan, Y.C., Zhang, P., Zhong, Q., Zhu, D.J. & Li, D.X. 2020 Characteristics of wall-attached motions in open channel flows. *Phys. Fluids* **32** (5), 055110.

Eaton, J.K. & Fessler, J.R. 1994 Preferential concentration of particles by turbulence. *Intl J. Multiphase Flow* **20**, 169–209.

Fernholz, H.H. & Warnack, D. 1998 The effects of a favourable pressure gradient and of the Reynolds number on an incompressible axisymmetric turbulent boundary layer. Part 1. The turbulent boundary layer. *J. Fluid Mech.* **359**, 329–356.

Foken, T., Göockede, M., Mauder, M., Mahrt, L., Amiro, B. & Munger, W. 2004 *Post-Field Data Quality Control*. Springer Netherlands.

Formenti, P., Caquineau, S., Desboeufs, K., Klaver, A., Chevaillier, S., Journet, E. & Rajot, J.L. 2014 Mapping the physico-chemical properties of mineral dust in western Africa: mineralogical composition. *Atmos. Chem. Phys.* **14** (19), 10663–10686.

https://doi.org/10.1017/jfm.2025.28 Published online by Cambridge University Press

GANAPATHISUBRAMANI, B., HUTCHINS, N., HAMBLETON, W.T., LONGMIRE, E.K. & MARUSIC, I. 2005 Investigation of large-scale coherence in a turbulent boundary layer using two-point correlations. *J. Fluid Mech.* **524**, 57–80.

GANAPATHISUBRAMANI, B., LONGMIRE, E.K. & MARUSIC, I. 2006 Experimental investigation of vortex properties in a turbulent boundary layer. *Phys. Fluids* **18** (5), 055105.

GINOUX, P., CHIN, M., TEGEN, I., PROSPERO, J.M., HOLBEN, B., DUBOVIK, O. & LIN, S.-J. 2001 Sources and distributions of dust aerosols simulated with the GOCART model. *J. Geophys. Res. Atmos.* **106** (D17), 20255–20273.

GUI, K. et al. 2022 Record-breaking dust loading during two mega dust storm events over northern China in March 2021: aerosol optical and radiative properties and meteorological drivers. *Atmos. Chem. Phys.* **22** (12), 7905–7932.

HAMZEH, N.H., KARAMI, S., OPP, C., FATTAHI, E. & JEAN-FRANÇOIS, V. 2021 Spatial and temporal variability in dust storms in the Middle East, 2002–2018: three case studies in July 2009. *Arab. J. Geosci.* **14** (7), 32.

HE, X.B. & LIU, H.Y. 2023 The effect of turbulent motions on particle spatial distribution in high-Reynolds-number particle-laden flows. *J. Fluid Mech.* **976**, A14.

HE, X.B., LIU, H.Y. & ZHENG, X.J. 2024 Wall-attached structure characteristics of flow and dust concentration fields in high-Reynolds-number particle-laden flows. *J. Fluid Mech.* **986**, A21.

HEINOLD, B., KNIPPERTZ, P., MARSHAM, J.H., FIEDLER, S., DIXON, N.S., SCHEPANSKI, K., LAURENT, B. & TEGEN, I. 2013 The role of deep convection and nocturnal low-level jets for dust emission in summertime West Africa: estimates from convection-permitting simulations. *J. Geophys. Res. Atmos.* **118** (10), 4385–4400.

HELFER, K.C. & NUIJENS, L. 2021 The morphology of simulated trade-wind convection and cold pools under wind shear. *J. Geophys. Res. Atmos.* **126** (20), e2021JD035148.

HELMERT, J., HEINOLD, B., TEGEN, I., HELLMUTH, O. & WENDISCH, M. 2007 On the direct and semidirect effects of Saharan dust over Europe: A modeling study. *J. Geophys. Res. Atmos.* **112** (D13), D13208.

HOMMEMA, S.E. & ADRIAN, R.J. 2003 Packet structure of surface eddies in the atmospheric boundary layer. *Boundary-Layer Meteorol.* **106** (1), 147–170.

HUTCHINS, N., CHAUHAN, K., MARUSIC, I., MONTY, J. & KLEWICKI, J. 2012 Towards reconciling the large-scale structure of turbulent boundary layers in the atmosphere and laboratory. *Boundary-Layer Meteorol.* **145** (2), 273–306.

HUTCHINS, N. & MARUSIC, I. 2007 Evidence of very long meandering features in the logarithmic region of turbulent boundary layers. *J. Fluid Mech.* **579**, 1–28.

JACOB, C. & ANDERSON, W. 2017 Conditionally averaged large-scale motions in the neutral atmospheric boundary layer: insights for aeolian processes. *Boundary-Layer Meteorol.* **162** (1), 21–41.

JIMÉNEZ, J. 2018 Coherent structures in wall-bounded turbulence. *J. Fluid Mech.* **842**, P1.

KAFTORI, D., HETSRONI, G. & BANERJEE, S. 1998 The effect of particles on wall turbulence. *Intl J. Multiphase Flow* **24** (3), 359–386.

KASKAOUTIS, D.G., FRANCIS, D., RASHKI, A., CHABOUREAU, J.P. & DUMKA, U.C. 2019 Atmospheric dynamics from synoptic to local scale during an intense frontal dust storm over the sistan basin in winter 2019. *Geosciences* **9** (10), 453.

KIM, K.C. & ADRIAN, R.J. 1999 Very large-scale motion in the outer layer. *Phys. Fluids* **11** (2), 417–422.

KNIPPERTZ, P. 2014 *Meteorological Aspects of Dust Storms*. Springer Netherlands.

KOVASZNAY, L.S., KIBENS, V. & BLACKWELDER, R.F. 1970 Large-scale motion in the intermittent region of a turbulent boundary layer. *J. Fluid Mech.* **41** (2), 283–325.

KROGSTAD, P.Å. & ANTONIA, R.A. 1994 Structure of turbulent boundary layers on smooth and rough walls. *J. Fluid Mech.* **277**, 1–21.

KRUG, D., BAARS, W.J., HUTCHINS, N. & MARUSIC, I. 2019 Vertical coherence of turbulence in the atmospheric surface layer: connecting the hypotheses of Townsend and Davenport. *Boundary-Layer Meteorol.* **172** (2), 199–214.

KUNKEL, G.J. & MARUSIC, I. 2006 Study of the near-wall-turbulent region of the high-Reynolds-number boundary layer using an atmospheric flow. *J. Fluid Mech.* **548**, 375–402.

LAMO, D.Á., J., C. & JIMÉNEZ, J. 2009 Estimation of turbulent convection velocities and corrections to Taylor's approximation. *J. Fluid Mech.* **640**, 5–26.

LAWRENCE, C.R. & NEFF, J.C. 2009 The contemporary physical and chemical flux of aeolian dust: a synthesis of direct measurements of dust deposition. *Chem. Geol.* **267** (1), 46–63.

LEE, J. & LEE, C. 2019 The effect of wall-normal gravity on particle-laden near-wall turbulence. *J. Fluid Mech.* **873**, 475–507.

https://doi.org/10.1017/jfm.2025.28 Published online by Cambridge University Press

LEE, J.H. & SUNG, H.J. 2011 Very-large-scale motions in a turbulent boundary layer. *J. Fluid Mech.* **673**, 80–120.

LI, X., HUTCHINS, N., ZHENG, X., MARUSIC, I. & BAARS, W.J. 2022 Scale-dependent inclination angle of turbulent structures in stratified atmospheric surface layers. *J. Fluid Mech.* **942**, A38.

LIM, J.Y. & CHUN, Y.S. 2006 The characteristics of Asian dust events in Northeast Asia during the springtime from 1993 to 2004. *Glob. Planet. Change* **52** (1), 231–247.

LIN, C.C. 1953 On Taylor's hypothesis and the acceleration terms in the Navier–Stokes equation. *Q. Appl. Maths* **10** (4), 295–306.

LIU, H.Y., BO, T.L. & LIANG, Y.R. 2017*a* The variation of large-scale structure inclination angles in high Reynolds number atmospheric surface layers. *Phys. Fluids* **29** (3), 035104.

LIU, H.Y., SHI, Y.X. & ZHENG, X.J. 2022 Evolution of turbulent kinetic energy during the entire sandstorm process. *Atmos. Chem. Phys.* **22** (13), 8787–8803.

LIU, H.Y., SHI, Y.X. & ZHENG, X.J. 2024 Scaling law of the second-order structure function over the entire sandstorm process. *J. Fluid Mech.* **978**, A29.

LIU, H.Y., WANG, G.H. & ZHENG, X.J. 2017*b* Spatial length scales of large-scale structures in atmospheric surface layers. *Phys. Rev. Fluids* **2** (6), 064606.

LIU, H.Y. & ZHENG, X.J. 2021 Large-scale structures of wall-bounded turbulence in single- and two-phase flows: advancing understanding of the atmospheric surface layer during sandstorms. *Flow* **1**, E5.

LIU, H.Y. & ZHENG, X.J. 2024 Buoyancy effects on very-large-scale motions and amplitude modulation in convective atmospheric surface layers. *Intl J. Heat Fluid Flow* **106**, 109327.

LIU, Y., JIANG, X., LEE, C. & HU, H. 2020 An experimental study on the spatiotemporal evolution of sand waves/ripples in turbulent boundary layer airflow. *Phys. Fluids* **32** (6), 063304.

LOTFY, E.R. & HARUN, Z. 2018 Effect of atmospheric boundary layer stability on the inclination angle of turbulence coherent structures. *Environ. Fluid Mech.* **18** (3), 637–659.

LOVETT, C., SOWLAT, M.H., SALIBA, N.A., SHIHADEH, A.L. & SIOUTAS, C. 2018 Oxidative potential of ambient particulate matter in Beirut during Saharan and Arabian dust events. *Atmos. Environ.* **188**, 34–42.

MAHOWALD, N.M., BAKER, A.R., BERGAMETTI, G., BROOKS, N., DUCE, R.A., JICKELLS, T.D., KUBILAY, N., PROSPERO, J.M. & TEGEN, I. 2005 Atmospheric global dust cycle and iron inputs to the ocean. *Glob. Biogeochem. Cycles* **19** (4), GB4025.

MARCHIOLI, C. & SOLDATI, A. 2002 Mechanisms for particle transfer and segregation in a turbulent boundary layer. *J. Fluid Mech.* **468**, 283–315.

MARUSIC, I. & HEUER, W.D.C. 2007 Reynolds number invariance of the structure inclination angle in wall turbulence. *Phys. Rev. Lett.* **99** (11), 114504.

MARUSIC, I., MCKEON, B.J., MONKEWITZ, P.A., NAGIB, H.M., SMITS, A.J. & SREENIVASAN, K.R. 2010 Wall-bounded turbulent flows at high Reynolds numbers: recent advances and key issues. *Phys. Fluids* **22** (6), 065103.

MARUSIC, I. & MONTY, J.P. 2019 Attached eddy model of wall turbulence. *Annu. Rev. Fluid Mech.* **51** (1), 49–74.

MAXEY, M.R. 1987 The gravitational settling of aerosol particles in homogeneous turbulence and random flow fields. *J. Fluid Mech.* **174**, 441–465.

MCLAUGHLIN, J.B. 1989 Aerosol particle deposition in numerically simulated channel flow. *Phys. Fluids A Fluid Dyn.* **1** (7), 1211–1224.

MIRI, A., MALEKI, S. & MIDDLETON, N. 2021 An investigation into climatic and terrestrial drivers of dust storms in the Sistan region of Iran in the early twenty-first century. *Sci. Total Environ.* **757**, 143952.

MOCKFORD, T., BULLARD, J.E. & THORSTEINSSON, T. 2018 The dynamic effects of sediment availability on the relationship between wind speed and dust concentration. *Earth Surf. Process. Landf.* **43** (11), 2484–2492.

MONCHAUX, R., BOURGOIN, M. & CARTELLIER, A. 2010 Preferential concentration of heavy particles: a Voronoï analysis. *Phys. Fluids* **22** (10), 103304.

MONTY, J.P., STEWART, J.A., WILLIAMS, R.C. & CHONG, M.S. 2007 Large-scale features in turbulent pipe and channel flows. *J. Fluid Mech.* **589**, 147–156.

MORRIS, S.C., STOLPA, S.R., SLABOCH, P.E. & KLEWICKI, J.C. 2007 Near-surface particle image velocimetry measurements in a transitionally rough-wall atmospheric boundary layer. *J. Fluid Mech.* **580**, 319–338.

NIU, Q.H., QU, J.J., ZHANG, K.C. & LIU, X.W. 2012 Thermodynamic effects on particle movement: wind tunnel simulation results. *Chinese Geogr. Sci.* **22** (2), 178–187.

PERRY, A.E., HENBEST, S. & CHONG, M.S. 1986 A theoretical and experimental-study of wall turbulence. *J. Fluid Mech.* **165**, 163–199.

https://doi.org/10.1017/jfm.2025.28 Published online by Cambridge University Press

PIOMELLI, U., BALARAS, E. & PASCARELLI, A. 2000 Turbulent structures in accelerating boundary layers. *J. Turbul.* **1**, N1.

ROBINSON, S.K. 1991 Coherent motions in the turbulent boundary layer. *Annu. Rev. Fluid Mech.* **23** (1), 601–639.

SALESKY, S.T. & ANDERSON, W. 2018 Buoyancy effects on large-scale motions in convective atmospheric boundary layers: implications for modulation of near-wall processes. *J. Fluid Mech.* **856**, 135–168.

SHAO, Y.P., KLOSE, M. & WYRWOLL, K.-H. 2013 Recent global dust trend and connections to climate forcing. *J. Geophys. Res. Atmos.* **118** (19), 1–12.

TALAMELLI, A., FORNACIARI, N., WESTIN, J.K.A. & ALFREDSSON, P.H. 2002 Experimental investigation of streaky structures in a relaminarizing boundary layer. *J. Turbul.* **3** (1), N18.

TALLURU, K.M., PHILIP, J. & CHAUHAN, K.A. 2018 Local transport of passive scalar released from a point source in a turbulent boundary layer. *J. Fluid Mech.* **846**, 292–317.

TAY, G.F., KUHN, D.C. & TACHIE, M.F. 2015 Effects of sedimenting particles on the turbulence structure in a horizontal channel flow. *Phys. Fluids* **27** (2), 025106.

TOWNSEND, A.A. 1976 *The Structure of Turbulent Shear Flow*. Cambridge University Press.

TUTKUN, M., GEORGE, W.K., DELVILLE, J., STANISLAS, M., JOHANSSON, P.B.V., FOUCAUT, J.M. & COUDERT, S. 2009 Two-point correlations in high reynolds number flat plate turbulent boundary layers. *J. Turbul.* **10**, N21.

VALLIKIVI, M., GANAPATHISUBRAMANI, B. & SMITS, A.J. 2015 Spectral scaling in boundary layers and pipes at very high Reynolds numbers. *J. Fluid Mech.* **771**, 303–326.

VOLINO, R.J., SCHULTZ, M.P. & FLACK, K.A. 2007 Turbulence structure in rough- and smooth-wall boundary layers. *J. Fluid Mech.* **592**, 263–293.

WANG, G.H., CHEN, W.B. & ZHENG, X.J. 2024 Experimental study of the effect of particle-wall interactions on inertial particle dynamics in wall turbulence. *J. Fluid Mech.* **984**, A4.

WANG, G.H., GU, H.H. & ZHENG, X.J. 2020 Large scale structures of turbulent flows in the atmospheric surface layer with and without sand. *Phys. Fluids* **32** (10), 106604.

WANG, G.H. & ZHENG, X.J. 2016 Very large scale motions in the atmospheric surface layer: a field investigation. *J. Fluid Mech.* **802**, 464–489.

WANG, P., FENG, S.J., ZHENG, X.J. & SUNG, H.J. 2019 The scale characteristics and formation mechanism of aeolian sand streamers based on large eddy simulation. *J. Geophys. Res. Atmos.* **124** (21), 11372–11388.

WYNGAARD, J.C. 1992 Atmospheric-turbulence. *Annu. Rev. Fluid Mech.* **24** (1), 205–233.

YANG, K., ZHAO, L. & ANDERSSON, H.I. 2017 Preferential particle concentration in wall-bounded turbulence with zero skin friction. *Phys. Fluids* **29** (11), 113302.

ZHANG, H. & ZHOU, Y.H. 2023 Unveiling the spectrum of electrohydrodynamic turbulence in dust storms. *Nat. Commun.* **14** (1), 408.

ZHANG, Y.Y., HU, R.F. & ZHENG, X.J. 2018 Large-scale coherent structures of suspended dust concentration in the neutral atmospheric surface layer: a large-eddy simulation study. *Phys. Fluids* **30** (4), 046601.

ZHOU, J., ADRIAN, R.J., BALACHANDAR, S. & KENDALL, T.M. 1999 Mechanisms for generating coherent packets of hairpin vortices in channel flow. *J. Fluid Mech.* **387**, 353–396.

ZHU, H.Y., PAN, C., WANG, G.H., LIANG, Y.R., JI, X.C. & WANG, J.J. 2021 Attached eddy-like particle clustering in a turbulent boundary layer under net sedimentation conditions. *J. Fluid Mech.* **920**, A53.

https://doi.org/10.1017/jfm.2025.28 Published online by Cambridge University Press